Observations of creep of polar firn at different temperatures

Yuan Li[1,3], Kaitlin Keegan[2], Ian Baker[1]

[1]Thayer School of Engineering, Dartmouth College, Hanover, NH, 03755, USA

[2]Department of Geological Sciences & Engineering, University of Nevada, Reno, Reno, NV, 89557, USA

[3]X-Here (Future ice-based Hydrogen energy & resilient environments) Trek Laboratory (Establishing), Howard Beach, NY, 11414, USA

Correspondence to: Ian Baker (ian.baker@dartmouth.edu)

Abstract

To improve our understanding of firn compaction and deformation processes, constant-load compressive creep tests were performed on specimens from a Summit, Greenland (72°35' N, 38°25' W) firn core that was extracted in June, 2017. Cylindrical specimens were tested at temperatures of –5°C, –18°C and –30°C from depths of 20 m, 40 m and 60 m at stresses of 0.21 MPa, 0.32 MPa and 0.43MPa, respectively. The microstructures were characterized before and after creep using both X-ray micro-computed tomography (micro-CT) and thin sections viewed between optical crossed polarizers. The results of these experiments comprise a novel data set on the creep of firn at three depths of a firn column at three different temperatures, providing useful calibration data for firn model development. Examining the resulting strain vs. time and strain vs. strain rate curves from the creep tests revealed the following notable features. First, the time exponent k was found to be 0.34–0.69 during transient creep, which is greater than the 0.33 usually observed in fully-dense ice. Second, the strain rate minimum (SRmin) in secondary creep occurred at a greater strain from specimens with lower density and at higher temperatures. Third, tertiary creep occurred more easily for the lower-density specimens at greater effective stresses and higher temperatures, where strain softening is primarily due to recrystallization. Fourth, the SRmin is a function of the temperature for a given firn density. Lastly, we developed empirical equations for inferring the SRmin, as it is difficult to measure during creep at low temperatures. The creep behaviors of polar firn, being essentially different from full-density ice, imply that firn densification is an indispensable process within the snow-to-ice transition, particularly firn deformation at different temperatures connected to a changing climate.

32   **Keywords:** Firn densification; Creep; Activation energy; Cryospheric micro-CT; Temperature

1. Introduction

Understanding firn compaction and densification experimentally is critical for developing physics-based firn models that are necessary for many glaciological applications. For example, such models are essential for reconstructing ice-core paleoclimate records by simulating the lock-in depth of gases and the smoothing of climate signals (Schwander et al., 1997; Goujon et al., 2003). They are also crucial for interpreting ice-mass changes from satellite altimetry data, as they allow for the accurate correction of firn air content and surface elevation changes not related to underlying ice dynamics (Ligtenberg et al., 2011; Simonsen et al., 2013). However, the firn models used for these applications are empirical and are known to perform poorly outside of their calibration range (Lundin et al., 2017). Thus, a better understanding of firn compaction is necessary to refine firn models for these important glaciological applications. Laboratory compressive experiments on firn and ice improve our understanding of their respective flow laws and advance the development of firn models under a range of conditions. The rheology of polycrystalline ice, particularly its temperature-dependent creep deformation, is a cornerstone of glaciological modeling. Numerous studies have established a robust framework for understanding ice deformation, primarily through laboratory creep experiments (e.g. Glen, 1955; Weertman, 1983; Budd and Jacka, 1989; Durham et al., 2001; Goldsby and Kohlstedt, 2001; Petrenko and Whitworth, 1999). This body of work has confirmed that ice creep is strongly governed by temperature, typically described by an Arrhenius relationship with a well-constrained activation energy for grain-scale processes like dislocation glide and climb (e.g. Jacka, 1984; Hooke, 2005). In contrast, the mechanical behavior of firn, the intermediate porous material between snow and glacial ice, remains comparatively poorly characterized, especially with respect to temperature.

The experimental observations are interpreted by drawing parallels between firn deformation and the mechanical properties of its constituent material, polycrystalline ice. This connection is formalized through a poromechanics approach, where the behavior of the porous firn is derived from that of the ice skeleton using continuum mechanics and homogenization principles (Scapozza and Bartelt, 2003; Gagliardini and Meyssonnier, 2000; Coussy, 2004; Hutter and Johnk, 2004; Srivastava et al., 2010; Theile et al., 2011). While numerous studies have investigated ice deformation (e.g. Steinemann, 1954; Maeno and Ebinuma, 1983; Li et al., 1996; Jacka and Li, 2000; Song et al., 2006a, 2006b, 2008; Treverrow et al., 2012; Hammonds and Baker, 2016, 2018) and firn deformation (e.g. Landauer, 1958; Mellor, 1975; Salm, 1982; Ambach and Eisner, 1985; Meussen et al., 1999; Bartelt and von Moos, 2000; Theile et al., 2011; Li and Baker, 2021, 2022a), existing firn data are sparse and fragmented. A critical knowledge gap persists in the systematic experimental quantification of firn's mechanical response across a broad range of temperatures. Temperature is a first-order control on firn densification and deformation rates, yet most laboratory studies have been conducted at a limited number of isothermal conditions, often focused on a single density or at temperatures near the melting point (e.g. Mellor, 1975; Maeno and Ebinuma, 1983). Consequently, there is a pronounced lack of experimental data necessary to derive the systematic activation energy for the creep of firn over its full density spectrum. This parameter is not merely a scalar but is likely a function of density, microstructure, and the dominant deformation mechanism (compaction versus shear), transitioning from grain-boundary sliding in low-density firn to dislocation creep in high-density firn and ice (Hammonds and Baker, 2018; Li, 2022; Li and Baker, 2022a). The absence of comprehensive, temperature-variable creep data for firn across its density range renders it insufficient for constraining the

77 temperature-dependence terms in modern, physics-based firn models. Our work fills this gap via

78 X-ray micro-computed tomography-analyzed mechanical examinations, e.g. a systematic series of

79 constant-stress creep experiments on firn cores of varying density, conducted across a thermally

80 controlled range from –30°C to –5°C. This allows for the direct determination whether the

81 apparent activation energy is a function of density, thereby providing the essential experimental

82 foundation needed to improve predictions of firn densification in ice-sheet and glacier models.

83 Notably, the mechanical behavior of two-phase flow coupling the airflow with the ice matrix

84 deformation has not yet been performed experimentally hitherto, even though the role of the

85 microstructures of firn on airflow has been studied (Albert et al., 2000; Courville et al., 2010;

86 Adolph and Albert, 2014). This difficulty is largely due to the limitations of the observation

87 techniques of nondestructive visualization of the microstructures during snow and firn

88 deformation. Thus, caution should be taken when extending the conclusions to ice sheet and

89 glacier scales from sample laboratory experiments. Macroscopically, the creep of firn obeys a

90 power-law dependence of the strain rate on the stress at constant stresses and temperature, similar

91 to that of full-density ice (Li and Baker, 2022a). Note that both the diffusivity and permeability of

92 the air in the pores (Albert et al., 2000; Courville et al., 2010; Adolph and Albert, 2014) impact

93 heat conduction of the ice matrix, and hence the grain growth. This is tightly tied to the

94 micro-mechanisms, e.g. grain-boundary and lattice diffusion of the ice crystals (Li and Baker,

95 2021), superplastic deformation and inter-particle sliding from dislocation motion in the ice necks

96 (Bartelt and Von Moos, 2000), and likely rearrangement of the ice particles (Perutz and Seligman,

97 1939; Anderson and Benson, 1963; Ebinuma and Maeno, 1987).

98

99   Through experiments on isotropic ice samples subjected to uni-axial compaction at octahedral

100   stresses of 0.1–0.8 MPa and temperatures from –45ºC to –5ºC, Jacka and Li (2000) determined

101   the mechanisms involved in the empirical *power-law flow*, which was derived by Glen (1955) for

102   stresses ranging from 0.1–1 MPa at temperatures spanning from –13ºC to the melting-point. They

103   found that dynamic recrystallization predominated at higher temperatures and stresses, whereas

104   crystal rotation governed at lower temperatures and stresses. Later, Goldsby and Kohstedt (2001)

105   found that ice could exhibit *superplastic flow*, which depends inversely on the grain size,

106   particularly for fine-grained ice, while both dislocation creep and basal slip-limited creep were

107   unrelated to the grain size at stresses of 0.1 MPa or less over a wide range of temperatures.

108   Moreover, Baker and Gerberich (1979) reported that the apparent activation energy for creep for

109   polycrystalline ice, which was derived from tests at constant stress and temperatures ranging from

110   –40ºC to –5ºC, increased with increasing volume fraction of inclusions (bubbles, impurities, dust,

111   and air clathrate hydrates). Such inclusions governed the evolution of grain size related to thermal

112   activations. The activation energies for the creep of snow and ice have been determined by a

113   number of authors, and values ranging from 58.6–113 kJ mol^{-1} were obtained under both uniaxial

114   and hydrostatic experiments for snow with a density of ~400 kg m^{-3} at –13.6ºC to –3.6ºC

115   (Landauer, 1958); 44.8–74.5 kJ mol^{-1} from snow with densities of 440–830 kg m^{-3} at –34.5ºC to –

116   0.5ºC (Mellor and Smith, 1966); ~72.9 kJ mol^{-1} for firn with a density of 320–650 kg m^{-3} at the

117   South Pole (Gow, 1969); 69 $\pm$ 5 kJ mol^{-1} for a mean snow density of 423 $\pm$ 8 kg m^{-3} at –19ºC to

118   –11ºC (Scapozza and Bartelt, 2003); the 78 kJ mol^{-1} from polycrystalline ice compression

119   deformation at a temperature of –10 ºC (Duval and Ashby, 1983); ~60 kJ mol^{-1} for artificial and

120   natural ice at the South Pole (Pimienta and Duval, 1987); and 78 $\pm$ 4 kJ mol^{-1} for monocrystal ice

121   at –20°C to –4.5°C and 75 ± 2 kJ mol^{-1} for bicrystal ice at –15°C to –4.5°C (Homer and Glen,

122   1978). In summary, the flow law of polycrystalline ice and firn depends on the effects of

123   recrystallization, grain size, inclusions (Mellor and Testa, 1969; Vickers and Greenfield, 1968;

124   Barnes et al., 1971; Baker and Gerberich, 1979; Goodman et al., 1981), and the temperature.

125

126   With advanced observation techniques, the relevant microstructural parameters of snow and firn

127   have been characterized by a number of scientists (Arnaud et al., 1998; Coleou et al., 2001; Flin et

128   al., 2004; Wang and Baker, 2013; Wiese and Schneebeli, 2017; Li, 2022). Using X-ray

129   micro-computed tomography (micro-CT), Li and Baker (2022b) characterized metamorphism

130   from snow to depth hoar under opposing temperature gradients. Only rarely has work been

131   performed on the co-effects of temperature and stress on the densification of firn while

132   simultaneously visualizing the microstructural changes using a micro-CT. For example, Schleef et

133   al. (2014) reported that densification under varying conditions of overburden stress and

134   temperature from natural and laboratory-grown new snow showed a linear relationship between

135   density and the specific surface area (SSA). To this end, the aim of our present work is to

136   investigate the temperature dependence of the creep of polar firn and relate this to the change of

137   microstructure determined using micro-CT studies on firn obtained from Summit, Greenland in

138   2017. As is well known, temperature is a key parameter affecting the flow of firn and ice, and

139   plays a determined role in their deformation, especially for polythermal and temperate glaciers.

140   Due to the great difficulty of analyzing firn and ice deformation with the presence of liquid water,

141   this work focuses on the firn creep from the dry snow zone, i.e., areas without meltwater, at

142   different temperatures.

143

2. Samples and measurements

2.1 *Samples*

Three cylindrical samples (22 ± 0.5 mm diameter; 50 ± 0.5 mm high) were produced at each of three depths of 20 m, 40 m and 60 m from the same 2017 Summit, Greenland firn core that was studied in Li and Baker (2022a). Both the densities and porosities of these above samples are typical of values in the snow-to-ice transition zone as introduced in Section 1. It is important to note that the reduction in effective stress with increasing depth is evident in samples taken from these three specified depths (**Appendix A**). Before creep testing, one cylindrical firn samples from each depth was stored at a temperature of –5 ± 0.5ºC, –18 ± 0.5ºC, and –30 ± 0.5ºC for two days to achieve thermal equilibrium (Li and Baker, 2022a). It's also important to note that firn is a heterogeneous material that can have variations in layering, fabric, grain size, and impurity concentration across short distances. Thus, care was taken to extract the three replicate samples from the core at each depth as closely as possible to reduce the variability in their initial conditions.

2.2 Creep measurements

Three home-built creep jigs were placed in individual Styrofoam boxes in three different cold rooms that were held at temperatures of –5 ± 0.5ºC, –18 ± 0.5ºC and –30 ± 0.5ºC. Each creep jig consists of an aluminum base plate and three polished aluminum-guide rails passing through linear bearings that hold the upper aluminum loading plate (**Figure 1**). A linear voltage differential transducer (LVDT-Omega LD-320: resolution of 0.025%; linearity error of ± 0.15%

165 of full-scale output), parallel to the three aluminum-guide rails, was located adjacent to the center

166 of the upper plate, and fixed firmly using a screw through the plate (**Figure 1**) for measuring the

167 displacement during a test. The displacement was logged every 5 seconds using a Grant SQ2010

168 datalogger (accuracy of 0.1%). Temperatures were logged at 300-second time intervals over the

169 entire test period, using a k-type thermocouple (Omega RDXL4SD thermistor: resolution of 0.1°C)

170 that was mounted inside each box. In this work, specimens were tested at temperatures of $-5 \pm$

171 0.2°C, -18 ± 0.2°C and -30 ± 0.2°C from depths of 20 m (applied stress 0.21 MPa), 40 m (0.32

172 MPa) and 60 m (0.43 MPa). There are smaller error bars for the temperature of the specimens

173 than the room temperature because the creep jigs were in insulated Styrofoam boxes. The stresses

174 were chosen based on experience from previous tests (Li and Baker, 2022a) in order to give

175 measurable creep rates in a reasonable time.

176
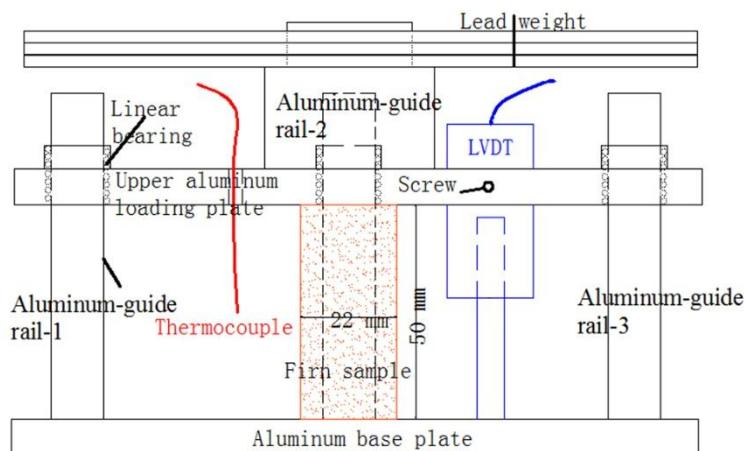
178 **Figure 1:** Schematic illustrating the home-built compressive creep jigs. More details can be found

179 in (Li & Baker, 2022a).

180

181

182 2.3 *X-ray micro-computed tomography (micro-CT)*

183 Each specimen at each depth and temperature combination was scanned using a Skyscan 1172

184 micro-CT, before and after creep testing. Each micro-CT scan lasted ~2 h. The cubic Volume of

185 Interest (VOI, a side length of 8 mm) was taken from near the center of the firn specimen as

186 conducted in Li and Baker (2022a). The microstructural parameters obtained from the micro-CT

187 data are the SSA, the mean structure thickness of the ice matrix (S.Th), the area-equivalent circle

188 diameter of the pores (ECDa), the total porosity (TP), the closed porosity (CP), and the structure

189 model index (SMI). The SSA (mm^{-1}) is the ratio of the ice surface area to total firn volume (ice

190 plus air) in a VOI analytical element, and is calculated using the hexahedral marching cubes

191 algorithm via CTAn software (Wang and Baker, 2013). It characterizes the thickness and

192 complexity of the firn microstructure. Changes in SSA indicate a change in free energy of the ice

193 surfaces, the decrease of which represents the occurrence of sintering-pressure. The S.Th (mm) is

194 the mean structure thickness of an ice matrix (Hildebrand and Ruegsegger, 1997), which

195 represents the characteristic size of an ice particle in the firn, where the ice particle consists of one

196 or many crystals or grains. It is measured based on the largest sphere diameter that encloses a

197 point in the ice matrix and is completely bounded within solid surfaces. The ECDa (mm) is the

198 diameter of a circle having the same area as the average for all pores in the VOI from the 2-D

199 binary images, indicative of the characteristic size for the void space (Adolph and Albert, 2014).

200 The TP (%) is the ratio of the pore volume, including both open and closed pores, to the total VOI.

201 The CP (%) is the ratio of the volume of the closed pores to the total volume of solid plus closed

202 pores volume in a VOI, while the open porosity (%) is the ratio of the volume of the open pores to

203 the total VOI. The SMI is calculated based on the dilation of a 3-D voxel model (Hildebrand and

204   Ruegsegger, 1997) $\mathrm{SMI} = 6\left(S' \times V\right)\big/S^2$, where S' is the change in the surface area due to

205   dilation, and V and S are the object volume and surface area, respectively. It indicates the

206   prevalent ice curvature, negative values of which represent a concave surface, e.g. the hollow air

207   structure surrounded by an ice matrix. The more negative the SMI value, the more spherical the

208   pore. Notably, the micro-CT-derived density of each specimen agrees well with the bulk density

209   measured using the mass-volume approach (Li and Baker, 2021).

210

211   *2.4 Thin section preparation and imaging*

212   Thin sections for optical photographs before and after creep testing were cut from bulk specimens,

213   one side of which was first smoothed with a microtome. This side was then frozen onto a glass

214   plate (100 × 60 × 2 mm) by dropping supercooled gas-free water along its edges. Its thickness

215   was reduced to ~2 mm by a band saw, and finally thinned further to a uniform thickness of ~0.5

216   mm using a microtome. Images were captured using a digital camera after each thin section was

217   placed on a light table between a pair of crossed polarizing sheets.

218

219   **3 Results and discussion**

220   3.1 *Microstructures before creep*

221   Increasing firn density with increasing depth from either of the –5°C, –18°C, and –30°C

222   specimens can be readily recognized by visual inspection of the micro-CT 3-D reconstructions of

223   the firn microstructure (**Figure 2**). Correspondingly, the microstructural parameters, with the

224   exception of the CP, changed monotonically with increasing depth at each temperature, e.g. the –

225   30°C samples increased in density from 591 ± 1.4 kg m^{-3}, to 683 ± 4.2 kg m^{-3}, to 782 ± 1.5 kg m^{-3},

226 decreased in SSA from 4.64 ± 0.04 mm^{-1}, to 3.3 ± 0.06 mm^{-1}, to 2.39 ± 0.01 mm^{-1}, and decreased

227 in TP from $35.6 \pm 0.05\%$, $25.6 \pm 0.4\%$, to $14.8 \pm 0.2\%$ at 20, 40, and 60 m, respectively (**Table 1)**.

228 These above changes are similar to those previously observed in this firn core (Li and Baker,

229 2022a), implying that the sintering-pressure mechanism plays a crucial role in the densification of

230 polar firn due to the increasing overburden of snow and firn with increasing depth. However, the

231 microstructures of the samples from the three temperatures at each depth show little variability

232 and do not monotonically change with temperature, e.g. at 20 m depth the -5°C, -18°C, and $-$

233 30°C samples having densities of 589 ± 1.3 kg m^{-3}, 615 ± 2.5 kg m^{-3}, and 591 ± 1.4 kg m^{-3}, and

234

| –5ºC | –18ºC | –30ºC |

20 m; Before Creep   20 m; Before Creep   20 m; Before Creep

235

20 m; After 12.7% Strain   20 m; After 3.3% Strain   20 m; After 1.2% Strain

236

40 m; Before Creep   40 m; Before Creep   40 m; Before Creep

237

40 m; After 19.3% Strain   40 m; After 4.3% Strain   40 m; After 1.2% Strain

238

60 m; Before Creep   60 m; Before Creep   60 m; Before Creep

239

60 m; After 11.5% Strain   60 m; After 1.8% Strain   60 m; After 0.8% Strain
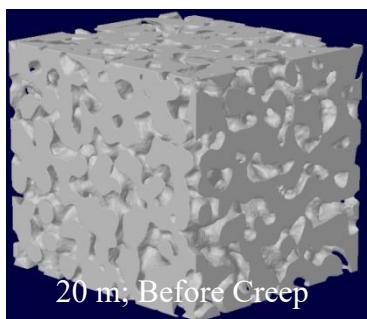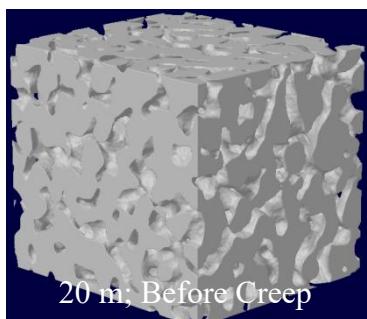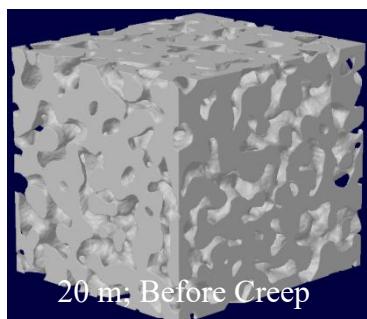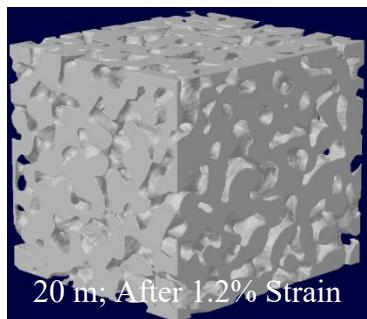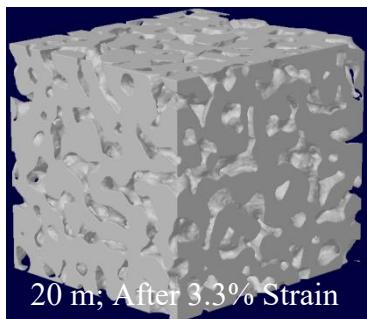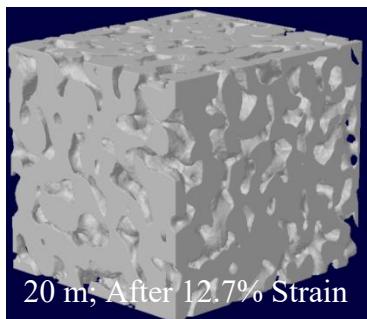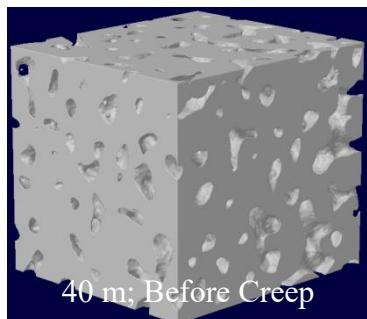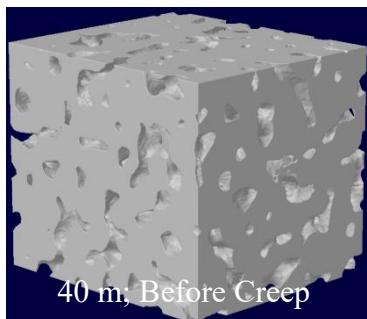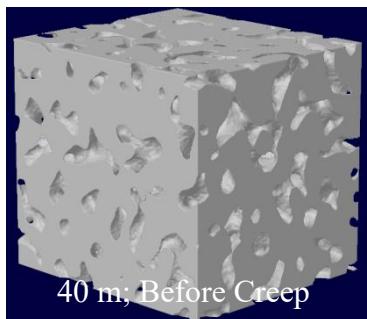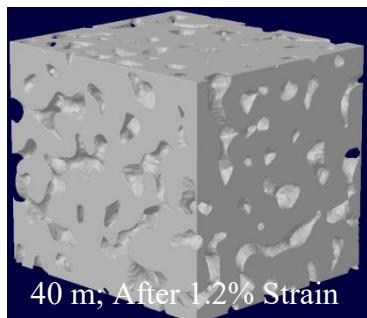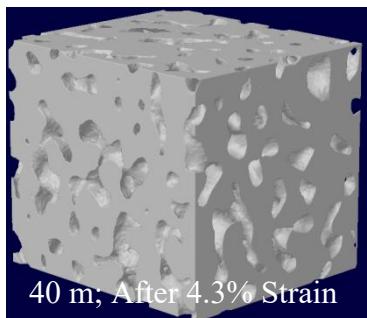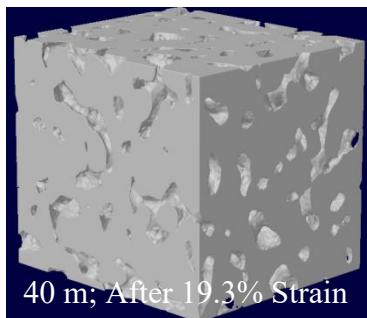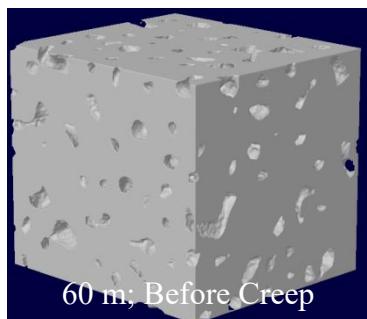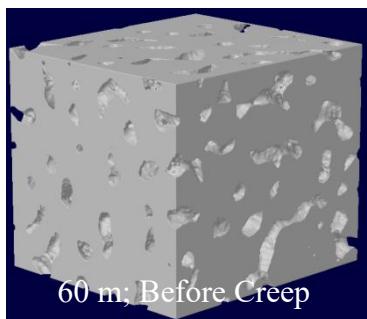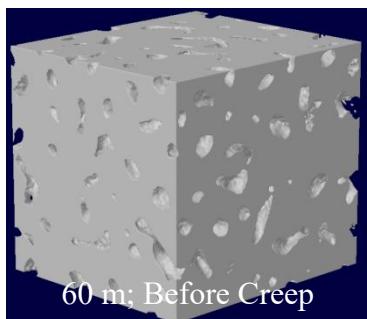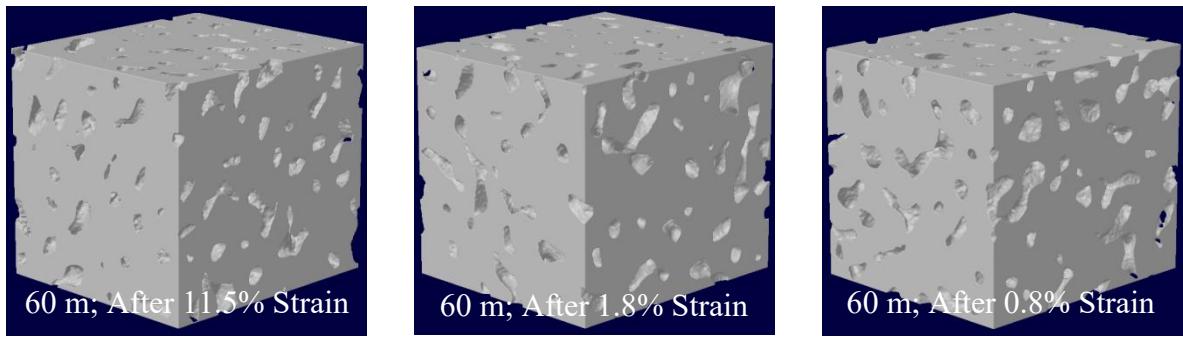
Figure 2: Micro-CT 3-D reconstructions (the side length of each cubic volume of interest is 8 mm) of specimens before and after creep testing at the depths and temperatures shown. Grey voxels represent ice in the firn structure.

Table 1. Microstructural parameters derived from Micro-CT for samples at –5ºC, –18ºC, and –30ºC from depths of 20 m, 40 m, and 60 m before creep.

20m							
T	Density	SSA	S.Th	TP	CP		ECDa
ºC	kg m^{-3}	mm^{-1}	mm	%	%	SMI	mm
–5	589±1.3	4.74±0.03	0.732±0.001	35.9±0.08	0.03±0.002	-0.31±0.04	1.07±0.005
–18	615±2.5	4.51±0.04	0.758±0.001	33.1±0.2	0.01±0.001	-0.57±0.01	0.995±0.013
–30	591±1.4	4.64±0.04	0.747±0.004	35.6±0.05	0.02±0.001	-0.27±0.05	1.09±0.004

40m							
T	Density	SSA	S.Th	TP	CP		ECDa
ºC	kg m^{-3}	mm^{-1}	mm	%	%	SMI	mm
–5	685±1.4	3.26±0.04	0.95±0.004	25.5±0.1	0.015±0.001	-1.85±0.11	0.857 ±0.005
–18	669±0.6	3.41±0.04	0.914±0.003	27.1±0.03	0.01±0.001	-1.69±0.09	0.892±0.002
–30	683±4.2	3.30±0.06	0.94±0.01	25.6±0.4	0.021±0.005	-1.87±0.13	0.86±0.01

60m							
T	Density	SSA	S.Th	TP	CP		ECDa
ºC	kg m^{-3}	mm^{-1}	mm	%	%	SMI	mm
–5	790±1.0	2.34±0.03	1.1±0.003	14.0±0.1	0.11±0.01	-4.81±0.22	0.594±0.003
–18	780±0.5	2.37±0.03	1.08±0.01	15.2±0.06	0.014±0.007	-4.8±0.2	0.632±0.001
–30	782±1.5	2.39±0.01	1.076±0.0003	14.8±0.2	0.02±0.001	-4.92±0.14	0.639±0.002

Note: SSA is the specific surface area, S.Th is the structure thickness, TP is the total porosity, CP

251 is the closed porosity, SMI is the structure model index, and ECDa is the area-equivalent circle

252 diameter.

253

254

255 SSAs of 4.74 ± 0.03 mm^{-1}, 4.51 ± 0.04 mm^{-1}, and 4.64 ± 0.04 mm^{-1}, respectively (**Figures 2–3**;

256 **Table 1**). Here, despite the -18°C specimen having a higher density than the two others at -5°C

257 and -30°C, is not possible to conclude that the sintering of firn is not directly related to the

258 temperature. This is likely because a thermal equilibration period of two days in the absence of

259 compression is too short to sufficiently exert the influence of temperature on firn sintering. The

260 microstructural differences seen in these specimens more likely arose from the initial samples

261 themselves, which were anisotropic and heterogeneous even if taken from the same depth,

262 attributed to firn pre-deformation and partial annealing before experiments (Li and Baker, 2022a).

263

264 3.2 *Microstructures after creep*

265 The microstructural evolution is characterized by the microstructural parameters shown in **Figure**

266 **3**. The largest changes occurred in the -5°C specimens due to the higher temperature, i.e., the

267 density, S.Th, and CP increased, while the ECDa, TP, SSA, and SMI decreased, indicative of

268 consolidation of the firn after creep. It is important to note that for the 60 m sample tested at -5°C,

269 there was no change in density, i.e., 790.2 ± 1 kg m^{-3} before creep vs. 790.7 ± 0.9 kg m^{-3} after

270 creep, or TP, i.e., $14.0 \pm 0.1\%$ before creep vs. $13.9 \pm 0.1\%$ after creep. This lack of

271 microstructural change is due to the high initial density, which was close to the firn pore close-off

272 density of ~830 kg m^{-3}. Thus, the creep of this sample may involve a transition from firn to

273 bubbly ice, as is also indicated by the increase in CP, which would have made it difficult to

274 compress further. Intriguingly, some of the changes in microstructure observed in the micro-CT

275 3-D reconstructions from the specimens before and after creep, e.g. the distribution of ice-space,

276 are indistinguishable in **Figure 2**. This is presumably due to the relatively large initial particle size,

277 or from radial dilation exceeding the axial compression because of the small strains that occurred

278 at relatively low temperatures.

279

280 One exception to the expected microstructural change after creep was the decrease of CP, which

281 was likely due to the measurement uncertainty of the micro-CT (Burr et al., 2018), or radial

282 expansion of the specimen during creep. Another exception was the decrease in density after

283 creep for the –18°C specimen at 20 m and the –30°C specimen at 60 m, which arose due to a

284 de-densification effect produced by temperature gradient metamorphism, as confirmed by the

285 increase of both TP and S.Th (Li and Baker, 2022b). The thermal gradient appears to be

286 associated with a fluctuation of 0.2°C around the test temperature, similar to temperature cycling

287 occurred within firn (Mellor and Testa, 1969; Weertman, 1985), which stems from the

288 thermometer's inherent accuracy as noted in Section 2.2 (–5 ± 0.2°C, –18 ± 0.2°C and –30 ±

289 0.2°C). In the relatively simple deformation found at ice-sheet dome sites, such as Summit, there

290 is no mechanism to decrease density during compression. At sites closer to the ice sheet margins,

291 cracking due to extension of the ice may cause a localized decrease in density. The rate of firn

292 densification should decrease with increasing depth at a given temperature, due to the decrease of

293 effective stress with increasing depth (**Appendix A**). As a matter of fact, the density of the –5°C

294 samples after creep increased by 32 kg m^{-3}, 44 kg m^{-3}, and 0.5 kg m^{-3} for the 20 m, 40

295

296
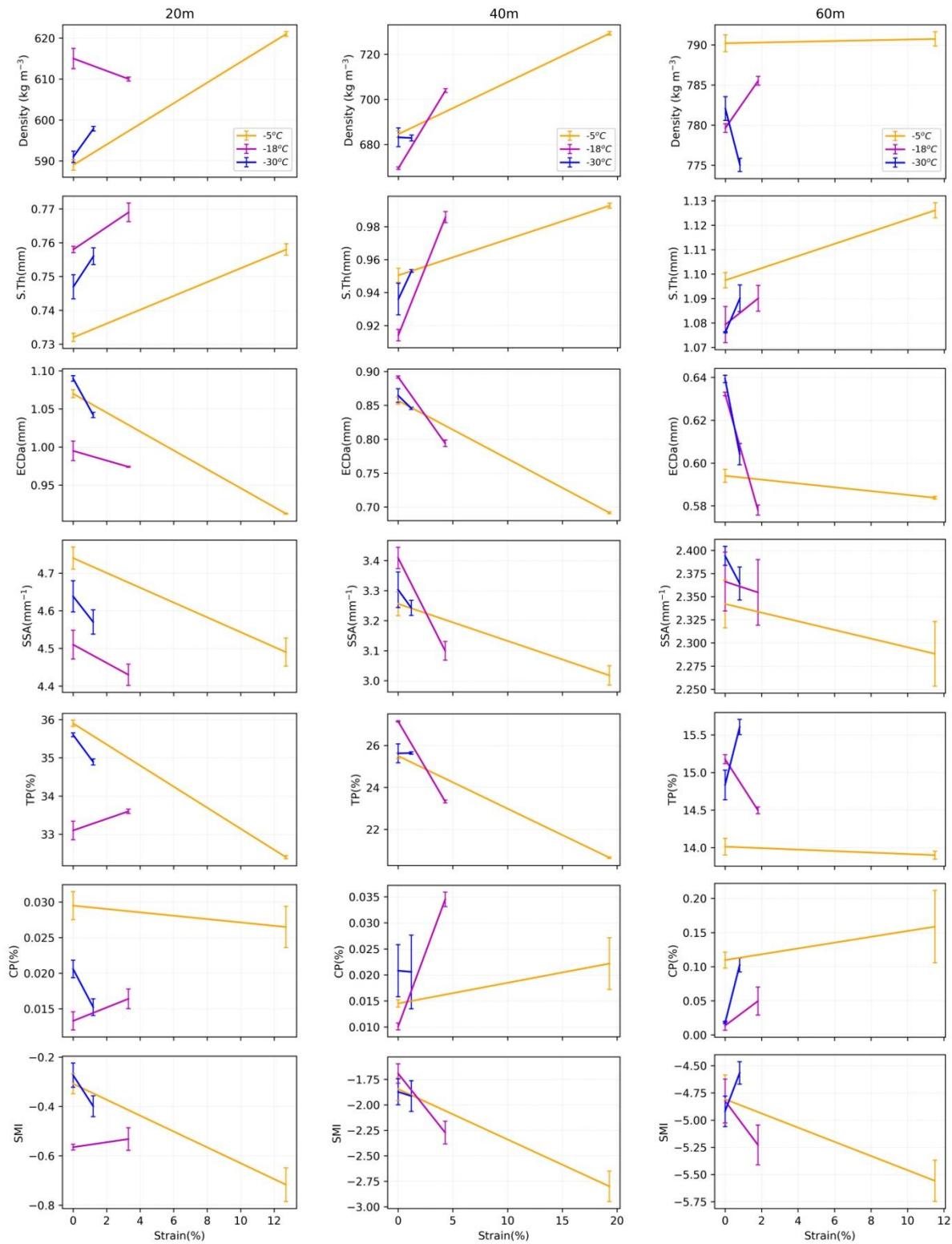
Figure 3: Density, structure thickness (S.Th), area-equivalent circle diameter (ECDa), specific

surface area (SSA), total porosity (TP), closed porosity (CP), and structure model index (SMI) of

299   the firn samples before and after creep at three temperatures (orange, magenta, and blue lines)

300   from depths of 20 m, 40 m and 60 m. Error bars indicate the variation of each microstructural

301   parameter as derived from three different VOIs of the same sample.

302

303

304   m, and 60 m samples, respectively. The 44 kg m^{-3} unexpectedly outnumbers the 32 kg m^{-3},

305   implying that the densification of firn is also affected by other undetermined factors, e.g. the

306   effect of inclusions, in addition to the stress and temperature.

307

308   Another way to investigate microstructure changes before and after creep tests is to compare their

309   grain sizes using thin sections. As an example, **Figure 4** shows optical micrographs of thin

310   sections made from the –5ºC sample at 40 m before and after creep to a strain of 19.3%, where

311   the significant reduction in grain size from 0.8 ± 0.67 mm to 0.5 ± 0.32 mm implies the

312   occurrence of recrystallization during testing. However, it is also unclear at what strain

313   recrystallization

314

315

316

317

318

319

320

321
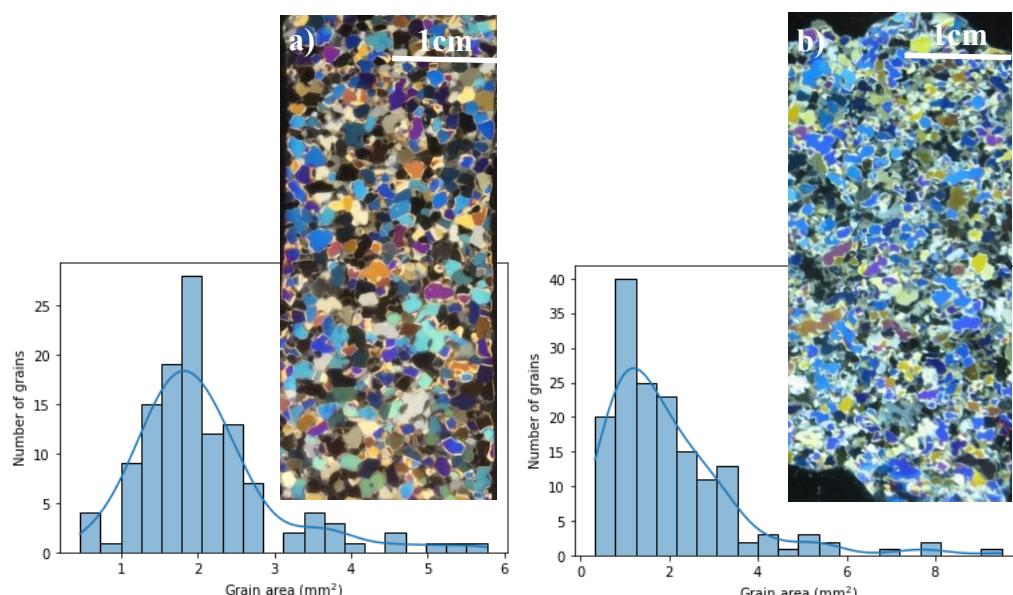
323   **Figure 4:** Optical micrographs of thin sections, and the distribution of grain sizes for the 40 m sample

324   at –5°C (a) before and (b) after creep (19.3% strain).

327   was initiated in each test, as noted in Li and Baker (2022a). Recrystallization occurs frequently at

328   a temperature higher than the homologous temperatures of 0.9 T_m. However, no evidence was

329   found for recrystallization after testing at the relatively cold –18°C and –30°C conditions,

330   probably due to the small creep strains at these relatively low temperatures. The creep

331   mechanisms for these samples, and whether the mechanisms were different at different

332   temperatures, could not be determined from the micro-CT-derived microstructural observations

333   alone, because the micro-CT can only capture the microstructure before and after creep. Instead,

334   plots of both strain vs. time and strain rate vs. strain can be used to elucidate the onset of

335   recrystallization during creep (Sections 3.3 and 3.4; Ogunmolasuyi, et al., 2023).

337   3.3 *Relationship between strain and time*

338   **Figure 5** shows the strain vs. time creep curves. The specimens at –5°C at 20 m and –18°C at 20

339   m, 40 m, and 60 m, show decelerating transient creep and quasi-viscous steady-state creep, while

340   the specimens at –5°C at 40 m and 60 m show transient, secondary, and accelerating tertiary creep.

341   Note that the curves from the –30°C specimens are not easily interpreted due to a large amount of

342   noise arising from both the insufficient resolution of a linear voltage differential transducer (Li

343   and Baker, 2022a) and the very small strains. The transient creep stage may be caused by strain

344 hardening that occurs from the yield point to the ultimate strength (Glen, 1955; Jacka, 1984). The

345 plastic deformation is accommodated by an increase in dislocation density through dislocation

346 multiplication or the formation of new dislocations (Frost and Ashby, 1982; Duval et al., 1983;

347 Ashby and Duval, 1985), which leads to an increase of the firn strength as the dislocations

348 become pinned or tangled, and thus more difficult to move. The initial decrease of creep rate may

349 also be related to the rearrangement of dislocations into a more stable pattern through a dragging

350 mechanism (Weertman, 1983) for the –5°C specimens. The tertiary creep stage may be associated

351 with strain softening deriving either from the thermally-activated processes at the high

352 homologous temperature approaching the melting point of ice, or from recrystallization (Li and

353 Baker, 2022a). Clearly, the creep rate of firn is sensitive to temperature under constant stress at a

354 given depth, *viz.*, the creep rate increases with increasing temperature (**Figure 5**). Incidentally,

355 there is no evidence of the onset of recrystallization in the creep curves themselves despite the

356 thin-section observation that –5°C specimens clearly underwent recrystallization during creep

357 (Section 3.2).

358

359 A modified Andrade-like equation $\varepsilon = \beta t^{k} + \varepsilon_0$ in Li and Baker (2022a) was used to describe the

360 transient creep behavior of the firn, in which the primary creep was well represented in black

361 dashed lines on the creep curves in **Figure 5**. The time exponent *k*, derived from the above

362 equation, ranges from 0.34–0.69: the data for the –30°C specimens are excluded since the noise in

363 the results makes them uninterpretable. These *k* values are also smaller than those from

364 monocrystalline and bicrystalline ice: 1.9 ± 0.5, 1.5 ± 0.2, and 1.3 ± 0.4 (Li and Baker, 2022a and

365 references therein). We also note that the *k* values from the specimens at –5°C from 20–60 m

366
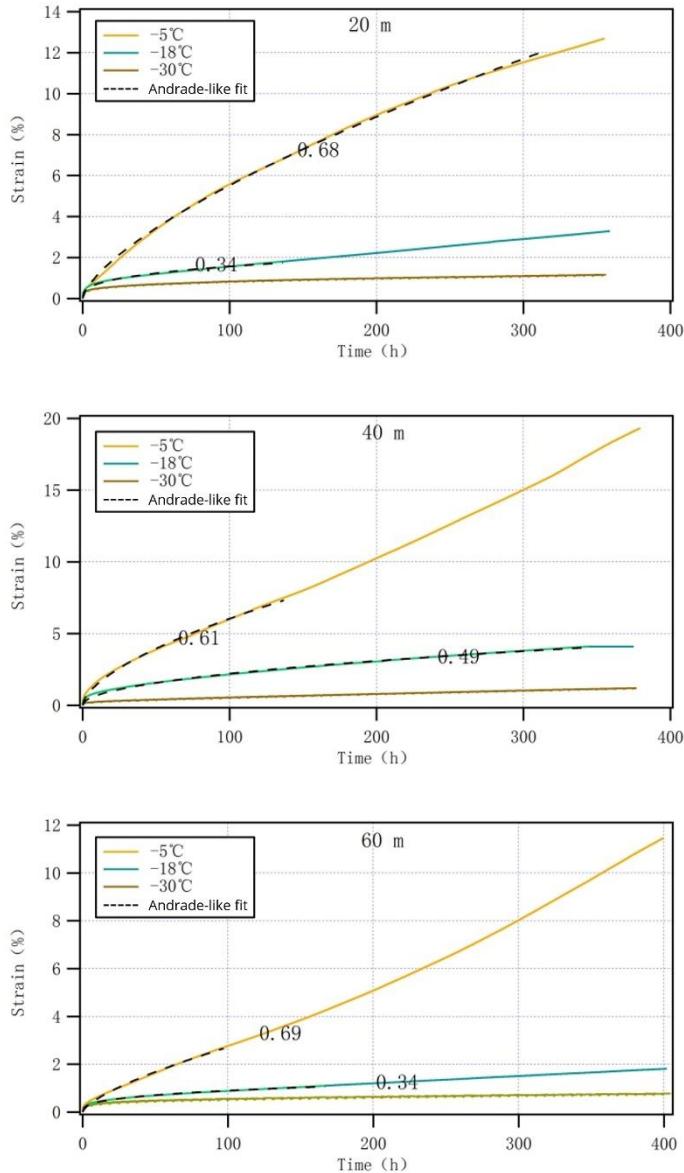
Figure 5: Strain vs. time for firn specimens at –5°C (yellow lines), –18°C (blue lines), and –30°C

(brown lines), from depths of 20 m (applied stress 0.21 MPa), 40 m (0.32 MPa) and 60 m (0.43

MPa). The black dashed curves represent fits to a modified Andrade-like equation with the time

exponents indicated on the curves, if any. Note: The *y*-axis limits vary across the subfigures.

(0.68, 0.61, and 0.69), and at –18°C from 40 m (0.49) are greater than 0.33, while the *k* value

from the –18°C specimens at 20 m (0.34) and 60 m (0.34) are close to 0.33 that is usually

375 obtained for full-density polycrystal ice. Interestingly, an evident relationship between the density

376 of firn and the k values, regardless of the effect of stress (Li and Baker, 2022a) and temperature,

377 remains unknown. A greater k value signifies faster deformation. The k values derived for firn are

378 generally higher than those for polycrystalline ice, implying that the higher firn deformation rates

379 compared to those of ice ($k = \sim0.33$; Cuffey and Paterson, 2010, and references therein) are likely

380 related to the fewer grain-boundary constraints with more void space in firn (Li and Baker, 2022a;

381 Li, 2023b). Clearly, the above k values, which increased with increasing temperature (**Figure 5**),

382 indicate that deformation is easier because of the lower viscosity at the higher temperature. Thus,

383 k seems to be a state variable with respect to temperature. In addition, k values greater than 0.33

384 may be related to the decrease of viscosity of the firn specimens (Freitag et al., 2002; Fujita et al.,

385 2014). k values lower than 0.33 observed under constant load and temperature occurred at

386 relatively low effective stresses (Li and Baker, 2022a). The identified trend of steadily declining k

387 values across the temperature range of –5°C to –18°C, however, represents a significant gap in

388 our current understanding, necessitating a dedicated investigation into the microstructural or

389 metamorphic causes. Alternatively, the enhanced cohesion strength in the firn, which resulted

390 from both the ice matrix with higher purity and the stronger bond connection of inter-grains,

391 increases the viscosity of test samples and lowers the k value to less than 0.33.

392

393 3.4 *Relationship of strain rate to strain*

394 **Figure 6** shows log strain rate vs. strain plots from all the –5°C and –18°C specimens; the –30°C

395 samples are excluded due to noise. The evolution of the strain rate is characterized more clearly in

396 **Figure 6** than in **Figure 5**. Clearly, the strain rate is also a state variable of temperature, where the

397   strain rate increases with increasing temperature for a given strain at a given depth (**Figure 6**;

398   **Table 2**). The strain rate minimum at the secondary creep stage (SRmin) and the strain at the

399

400

401   Table 2. Observed and inferred strain rate minima and strains observed at the strain rate minima.

20 m	SRmin s^{-1}	PC1-SRmin s^{-1}	PC2-SRmin s^{-1}	PC3-SRmin s^{-1}	Strain %
–5°C	5.53×10^{-6}	*5.53×10^{-6}*	*1.68×10^{-6}*	*2.56×10^{-7}*	11.8
–18°C	1.36×10^{-6}	*1.36×10^{-6}*	*2.29×10^{-7}*	*2.45×10^{-8}*	1.81–2.9
–30°C(U)	–	7.14×10^{-7}	2.17×10^{-7}	3.3×10^{-8}	–
–30°C(L)	–	3.16×10^{-8}	9.6×10^{-9}	1.46×10^{-9}	–

402

40 m	SRmin s^{-1}	PC1-SRmin s^{-1}	PC2-SRmin s^{-1}	PC3-SRmin s^{-1}	Strain %
–5°C	1.03×10^{-5}	*3.39×10^{-5}*	*1.03×10^{-5}*	*1.57×10^{-6}*	7.5
–18°C	1.4×10^{-6}	*8.32×10^{-6}*	*1.40×10^{-6}*	*1.5×10^{-7}*	4.1
–30°C(U)	–	4.37×10^{-6}	1.33×10^{-6}	2.03×10^{-7}	–
–30°C(L)	–	1.94×10^{-7}	5.88×10^{-8}	8.97×10^{-9}	–

403

60 m	SRmin s^{-1}	PC1-SRmin s^{-1}	PC2-SRmin s^{-1}	PC3-SRmin s^{-1}	Strain %
–5°C	5.59×10^{-6}	*1.21×10^{-4}*	*3.67×10^{-5}*	*5.59×10^{-6}*	2.7
–18°C	5.33×10^{-7}	*2.96×10^{-5}*	*4.99×10^{-6}*	*5.33×10^{-7}*	1.1–1.8
–30°C(U)	–	1.56×10^{-5}	4.74×10^{-6}	7.21×10^{-7}	–
–30°C(L)	–	6.91×10^{-7}	2.1×10^{-7}	3.19×10^{-8}	–

404   The SRmin without the prefix is the observed values during creep, while the SRmin with a prefix

405   is the inferred values. Note that PC-SRmin is the abbreviation of the post-calibration SRmin, and

406   that –30°C(U) and –30°C(L) indicate the upper and lower bound from the –30°C samples from

407   44.8 kJ mol^{-1} and 113 kJ mol^{-1}, respectively. PC1-SRmin, PC2-SRmin, and PC3-SRmin are

408   described in **Appendix B**. The symbol – indicates the unavailable values of SRmin and the strain

409   value at the SRmin observed during creep. For the italics highlighted, see **Appendix B**.

410

411
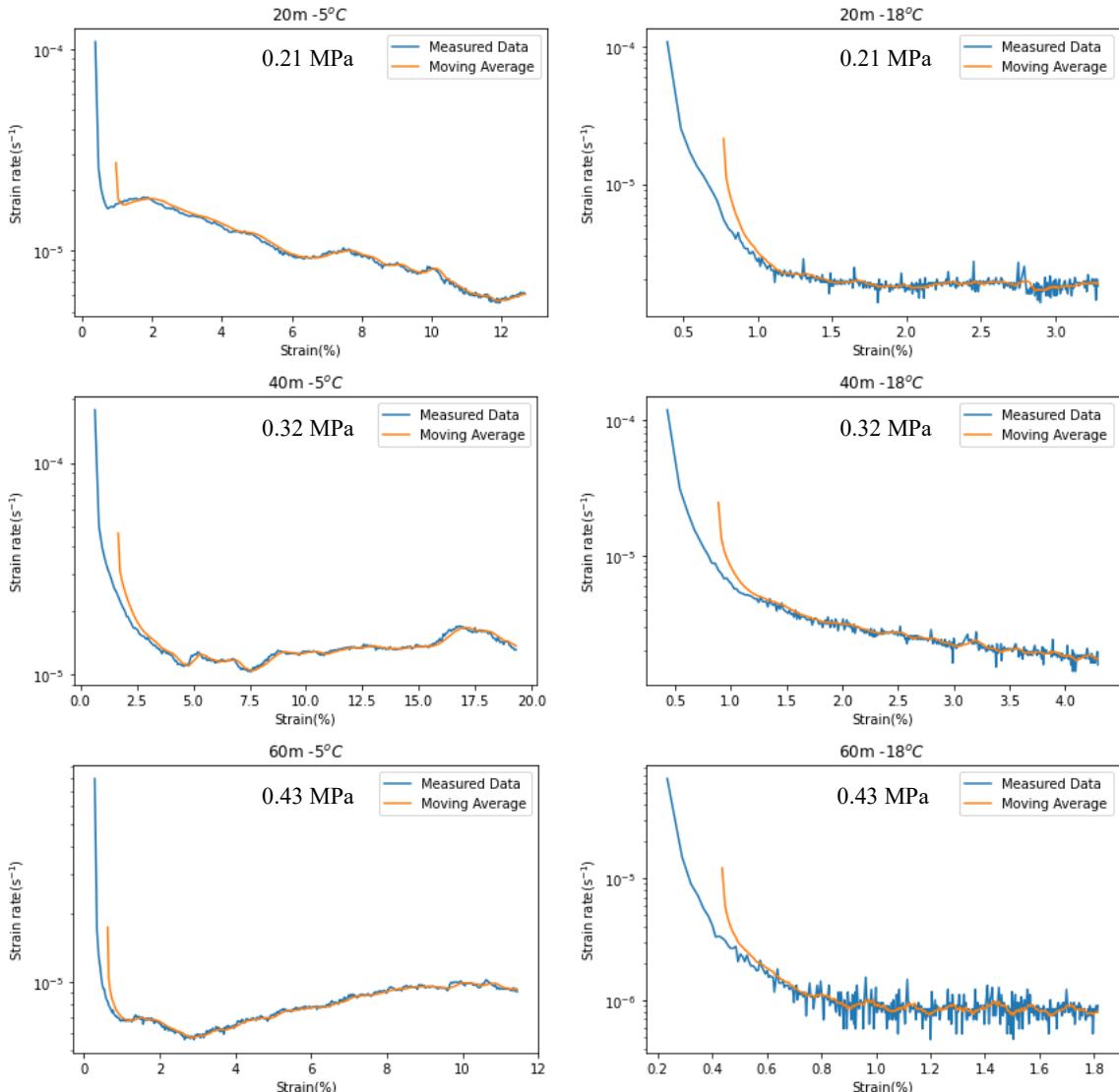
Figure 6: Log strain rate vs. strain from the firn specimens at temperatures of -5°C and -18°C

from depths of 20 m (applied stress 0.21 MPa), 40 m (0.32MPa) and 60 m (0.43MPa). Samples

from -30°C are not shown due to the very large noise. The blue lines represent discrete strain rates,

which are calculated by extracting the strain data hourly, while the orange lines represent a

moving average of 15 moving windows with respect to the strain.

420

421

422   SRmin for all the –5ºC and –18ºC specimens are shown in **Figure 6** and **Table 2**. The SRmin was

423   reached at a strain of 11.8%, 7.5% and 2.7% for the –5ºC specimens from depths of 20 m, 40 m,

424   and 60 m, respectively, consistent with strains at the SRmin decreasing with increasing depth at a

425   given temperature in **Figure 8** and **Table 4** in Li and Baker (2022a). For the –18 ºC specimens,

426   the SRmin occurred over a range of strains from 1.81–2.9% at 20 m, at a fixed strain of 4.1% at

427   40 m, and at a strain oscillating between 1.1 and 1.8% at 60 m. These values of strain at different

428   SRmin values are different from those usually observed at strains of 0.5–3% for fully-dense ice

429   (Cuffey and Paterson, 2010, and references therein), implying different mechanical behavior

430   between firn and pure ice (Duval, 1981; Mellor and Cole, 1983; Jacka, 1984; Li et al., 1996;

431   Jacka and Li, 2000; Song et al., 2005, 2008; Cuffey and Paterson, 2010). Overall, the strain at the

432   SRmin is greater with lower density and higher temperature, e.g. 11.8% strain from the –5ºC

433   specimens at 20 m, and 4.1% strain from the –18ºC specimens at 40 m. This is likely due to the

434   effect of strain hardening on density and temperature (Li, 2023b). Additionally, tertiary creep is

435   observed during both quasi-steady state deformation, particularly in the –5°C specimens at depths

436   of 40 m and 60 m, and in the ascending stage, as seen in the –5°C and –18°C specimens at 20 m,

437   along with the –18°C specimen at 40 m. This mechanical behavior is facilitated by lower firn

438   density, increased effective stress, and elevated creep temperatures. For instance, in the –5°C

439   specimens at 20 m, strain softening primarily results from recrystallization (Duval, 1981; Jacka,

440   1984; Jacka and Li, 2000; Song et al., 2005; Faria et al., 2014). Also, the activation of easy slip

441   systems contributes to this process (Jonas and Muller, 1969; Duval and Montagnat, 2002; Alley et

442   al., 2005; Horhold et al., 2012; Fujita et al., 2014; Eichler et al., 2017; Vedrine et al., 2025). It is

443   noteworthy that Jacka and Li (1994) observed that steady-state tertiary ice creep, which is marked

444   by stable grain size, is influenced more by applied stresses than by temperature. This finding

445   suggests that there exists a balance between the activation energies required for grain growth and

446   subdivision at a specific temperature.

447

448   3.5 *Apparent activation energy for creep*

449   Experimental observations of the SRmin are limited, as they only occurred for the –5°C and at –

450   18°C specimens at each depth (**Table 2**). It is hard to achieve the SRmin for all firn specimens in

451   laboratory environments (Landauer, 1958), especially under low temperatures and stresses such as

452   those from the –30°C specimens in this work. To this end, we offer the various possibilities of the

453   SRmin using the evidence we have. The value of the apparent activation energy of creep, Q_c (kJ

454   mol^{-1}), is equal to the slope of a line fitted $\ln \dot{\varepsilon}$ versus $1/T$ as did in Goldsby & Kohlstedt (1997;

455   2001), using the Arrhenius relation $\dot{\varepsilon} = B\sigma^n \exp(-\frac{Q_c}{RT})$, where $\dot{\varepsilon}$ (s^{-1}) is the strain rate, B (s^{-1}

456   Pa^{-n}) is the material parameter, σ (MPa) is the applied stress, n is the creep (stress) exponent, R

457   (8.314 J mol^{-1} K^{-1}) is the gas constant, and T (K) is Kelvin temperature. It is noted that under

458   constant-stress conditions, the value of the stress exponent n influences the pre-exponential factor

459   B but does not affect the slope of the Arrhenius plot and therefore the derived activation energy Q_c.

460   First, the estimation of Q_c is based on *only* two SRmin values from the –5°C and –18°C samples

461   at each depth (**Table 2**). Glen-King's model $\dot{\varepsilon} = A\exp(-Q_c/RT) = B\sigma^n \exp(-Q_c/RT)$ treats the

462   pre-factor A, material parameter B, and stress exponent n as constants (Glen, 1955; Goldsby and

463   Kohlstedt, 2001). This simplification is valid by using the unifying concept of normalized

464   effective stress. The effective stress captures the complex multi-physical behavior of the

465   two-phase ice-air system, accounting for: 1) The incompressibility of individual ice grains versus

466   the compressibility of the porous ice skeleton, 2) The coupled flow of ice and air; and 3) The

467   interplay between different strain components (axial, radial, volumetric, and true). This

468   framework is grounded in the principles of poromechanics, originally developed for soils and

469   later applied to snow and ice (Gubler, 1978; Hansen and Brown, 1988; Mahajan and Brown, 1993;

470   Chen and Chen, 1997; Lade and deBoer, 1997; Ehlers, 2002; Khalili et al., 2004; Gray and

471   Schrefler, 2007; daSilva et al., 2008; Nuth and Laloui, 2008). The variability in density for the

472   samples from 20-m depth on the mechanical behavior are negligible due to a small difference (up

473   to ~4%), between samples, which falls within an acceptable error range in previous studies. This

474   is likely related to multiple factors, including the intrinsic properties of the samples, e.g.

475   inclusions (impurities, dust, bubbles, clathrate hydrates), the effects of deformation and partial

476   annealing of firn due to stress distribution and temperature changes during drilling, extraction,

477   transportation, or storage, and the fact that the samples are taken from adjacent parts of the core,

478   and might capture heterogeneous density layers, as well as potential measurement errors

479   associated with the equipment used. The Q_c values from the 20 m, 40 m, and 60 m specimens

480   were calculated to be 61.4 kJ mol^{-1}, 87.3 kJ mol^{-1}, and 102.8 kJ mol^{-1}, respectively (**Figure 7**).

481   Based on the three SRmin from the –5°C and –18°C samples at 60 m in this work, and from –

482   10°C samples at 60 m in Li and Baker (2022a), a Q_c value for the 60 m specimen was calculated

483   to be 100.7 kJ mol^{-1}. To see whether or not these above Q_c values are reliable, we estimated the

484   activation energy of grain-boundary diffusion/viscosity, Q_{gbd} (kJ mol^{-1}), using the relation

485    $K = \left(D_t^2 - D_0^2 \right) / t = k \exp(-Q_{gbd}/RT)$, in an alternative form of $Q_{gbd} = -R\left[\partial \ln K / \partial \left(1/T \right) \right]$,

486   where K is the observed rate of grain growth (mm^2 a^{-1}), D_0^2 and D_t^2 are the measured mean

487   grain area (mm^2) in a firn sample at the onset of the creep ($t = 0$), and at the end time of the creep

488 (*t*-year), and *k* is a constant grain growth factor. The grain growth rates are plotted on a

489 logarithmic scale against the reciprocal of *T* (**Figure 7**). For changes in grain size from the related

490 specimens before and after creep see **Table 3**. Correspondingly, the Q_{gbd} values calculated were

491 41.4 kJ mol^{-1}, 40.8 kJ mol^{-1}, and 40.9 kJ mol^{-1} for the specimens at 20 m, 40 m, and 60 m,

492 respectively. These Q_{gbd} values are comparable to the values of 40.6 kJ mol^{-1} obtained in

493 laboratory experiments on polycrystalline ice (Jumawan, 1972), and 42.4 kJ mol^{-1} from 13 polar

494 firn cores (Cuffey and Paterson, 2010) for grain-boundary self-diffusion of polycrystalline ice.

495 Further, the ratio of Q_{gbd}/Q_c is 0.67, 0.47, and 0.4 for the 20 m, 40 m, and 60 m specimens,

496 respectively. We noted that the ratio of 0.67 for Q_{gbd}/Q_c was recommended by Hobbs (1974) and

497 Cuffey and Paterson (2010). The Q_c values calculated using the Arrhenius relation for the 40 m

498 and 60 m specimens are likely greater than the actual values, and hence are seemingly less

499 reliable. There is little difference between the two-SRmin-derived Q_c value (102.8 kJ mol^{-1}) and

500 the three-SRmin-derived Q_c value (100.7 kJ mol^{-1}), implying that these two avenues for

501 calculating Q_c have equal utility. Moreover, the above Q_{gbd} values are lower than the 48.6 kJ

502 mol^{-1} that was inferred by the grain growth rate for firn samples with densities ranging from 320–

503 650 kg m^{-3} from cores drilled at the South Pole, Antarctic (Gow, 1969), which makes a ratio of

504 0.67 for Q_{gbd}/Q_c an unreliable sole-criterion. In short, it is difficult to assess the reliability of both

505 Q_c and Q_{gbd}, as discussed above due to their scatter and debates in the current literature. Thus,

506 these Q_c values estimated in this work, ranging from 61.4–102.8 kJ mol^{-1}, are reasonable,

507 aligning with the literature range of 44.8–113 kJ mol^{-1} (**Table 4**).

508

509

Table 3. Grain area (mm^2) measured from optical thin sections for samples at –5ºC, –18ºC, and –30ºC from depths of 20 m, 40 m, and 60 m before and after creep.

Depth	20 m		40 m		60 m	
T/ºC	Before	After	Before	After	Before	After
–5	0.29±0.25	0.42±0.28	0.53±0.32	0.79±0.67	0.78±0.67	0.97±0.8
–18	0.29±0.25	0.34±0.2	0.53±0.32	0.7±0.42	0.78±0.67	0.9±0.59
–30	0.29±0.25	0.31±0.17	0.53±0.32	0.57±0.34	0.78±0.67	0.81±0.56

A great challenge is the estimation of the Q_c using the SRmin including the –30ºC specimens, whose SRmin shows high variability due to the extraordinarily slow strain rate at low temperatures. This difficulty cannot be resolved by extrapolating experimental data (Sinha, 1978; Hooke et al., 1980), e.g. the use of Andrade's law (Glen, 1955). Instead, we turned our focus to studying the relationship between the SRmin and temperature by constraining our data in a wide range of Q_c values reported in existing literature presented in **Table 4**. Clearly, there is a larger scatter of Q_c values for firn than for ice. The increase of Q_c from mono-crystalline and bi-crystalline to polycrystalline ice implies that the greater the reduction in the constraint from grain boundaries, the greater is Q_c. Alternatively, firn creep is easier than that of polycrystalline ice due to either the easier sliding of grains in firn along more directions in the more porous and heterogeneous structure (Section 3.3), or the decrease of viscosity associated with inclusions (e.g.
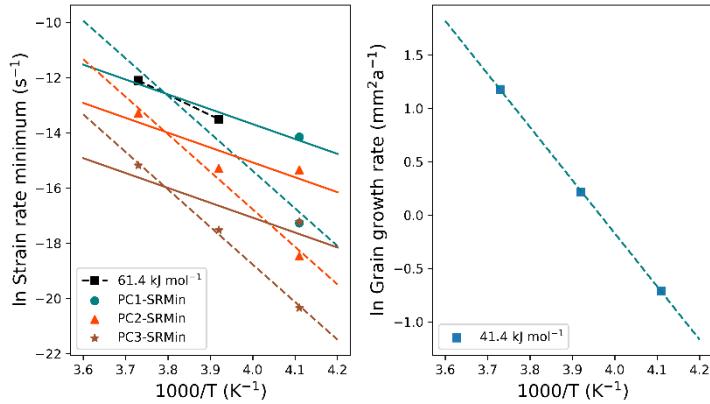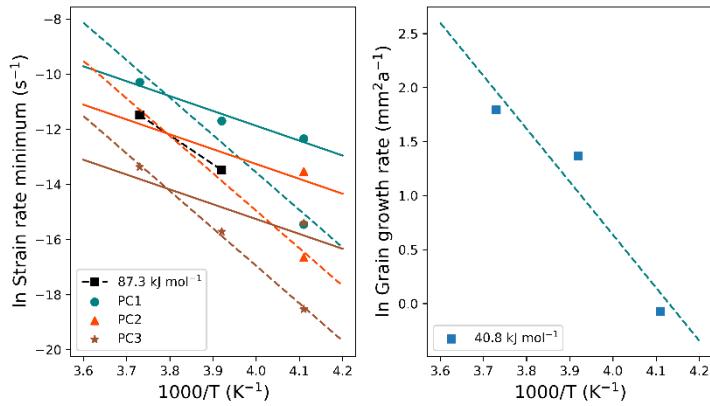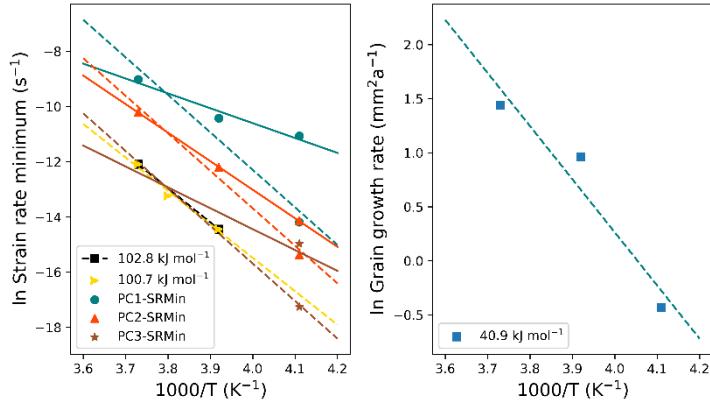
Figure 7: Arrhenius plots to estimate the apparent activation energy of creep (Q_c; left panel) and the apparent activation energy of grain-boundary diffusion (Q_{gbd}; right panel) from the firn specimens noted. The teal, orange, and brown solid lines are the upper bound (44.8 kJ mol⁻¹) of PC1-SRmin, PC2-SRmin, and PC3-SRmin, respectively, while the teal, orange, and brown dashed

534   lines are the lower bound (113 kJ mol^{-1}) of PC1-SRmin, PC2-SRmin, and PC3-SRmin,

535   respectively (Table 2). The teal circles, the orange triangles, and the brown stars are the data in

536   Table 2. The black dashed lines are from *only* two SRmins at –5°C and –18°C (the black squares

537   are the data measured), whose Q_c is indicated in each subfigure. The yellow dashed line is from

538   the three SRmins at –5°C, –18°C in this work, and –10 °C from Li and Baker (2022a) (the yellow

539   triangles are the measured data), whose Q_c is 110.7 kJ mol^{-1}. The blue dashed lines (right panel)

540   are from grain growth rate at three temperatures (the blue squares are the observed data), whose

541   Q_{gbd} is indicated in each subfigure.

542

543

544   Table 4. Apparent activation energy for the creep of firn and ice, Q_c, reported in literature.

Q_c kJ mol^{-1}	Sample	Density kg m^{-3}	Temperature °C	Methods	Source
58.6–113	Firn	~400	[–13.6, –3.6]	Uniaxial/Hydrostatic Compression	Landauer (1958)
44.8–74.5	Firn/Bubbly Ice	440–830	[–34.5, –0.5]	Uniaxial Unconfined Compression	Mellor and Smith (1966)
54	Firn/Bubbly Ice	Undetailed	[−28, −16]	Shear Deformation of Boreholes	Paterson (1977)
~72.9	Firn	320–650	Unnecessary	Grain Growth Rate	Gow (1969)
69 ± 5	Firn	423 ± 8	[–19, –11]	Triaxial Compression	Scapozza and Bartelt (2003)
~60	Artificial/Natural Ice (South Pole)	~917	–15	Torsion Creep Test	Pimienta and Duval (1987)
61	Polycrystalline Ice	~917	–9.6	Hydrostatic Pressure	Duval et al. (1983)
78	Monocrystalline Ice	~917	[–30, –4]	Derived from Bicrystal Ice	Homer and Glen (1978)
75	Ice Bicrystal	~917	[–30, –4]	Tensile Test Parallel to Grain-boundary	Homer and Glen (1978)

545

547 Baker and Gerberich, 1979; Goodman et al., 1981) that facilitate the intra- and inter-grain sliding

548 (Salamatin et al., 2009). In principle, Q_c of firn should exceed that for polycrystalline ice.

549 Intriguingly, some reported Q_c values from firn are less than that for ice, meaning the degree of

550 spatial freedom in the ice-matrix is limited by the topological structure of the firn (Liu et al.,

551 2022). Incidentally, the effective stress of porous materials is determined by not only its porosity,

552 but also other factors, e.g. the microstructural topology (Liu et al., 2022) and the impurity types

553 and concentrations in the firn. However, this issue is beyond the scope of this work. In seeking a

554 conclusion, we evaluated the dependence of creep activation energy on firn density. The data

555 indicate no discernible relationship between these two parameters (**Fig. 8**). In summary, a Q_c for

556 firn, which ranges from 44.8–113 kJ mol^{-1}, is plausible due to the intrinsic nature of natural firn

557 that has a far more complicated and changeable microstructure than ice.

558
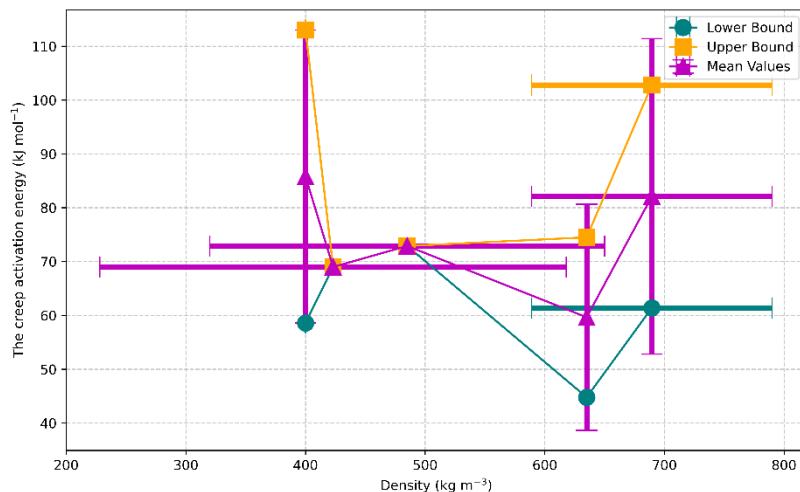
559

560 **Figure 8:** Plots of the creep activation energy vs. firn densities. For each density, three values are

561 shown: the lower bound (minimum activation energy, teal), the upper bound (maximum activation

562 energy, orange), and the mean value (magenta). Error bars represent the standard deviation of the

563   mean. Data are sourced from Table 4 and the present study.

564

565

566   The value of the stress exponent n is determined by plotting the line fit the logarithm relation of

567   the steady-state strain rate, $\dot{\varepsilon}$, versus the effective stress, σ, and is, thus, the slope of this line

568   from the measured SRmins (**Table 2**). We determined stress exponent (n) values of approximately

569   0.1 and –1.2 for the –5°C and –18°C samples based on observed data, respectively. This result

570   directly contradicts the value of $n \approx 4.3$ reported from the same Greenland firn core by Li and

571   Baker (2022a). Further, these values fall entirely outside the established range of ~1 to ~7.5

572   (mean ~4.25 ± 3.25) documented across decades of ice mechanics literature (Glen, 1955; Hansen

573   and Landauer, 1958; Butkovich and Landauer 1960; Kamb, 1961; Paterson and Savage, 1963;

574   Higashi et al, 1965; Mellor and Testa, 1969; Raymond, 1973; Hooke, 1981; Thomas et al., 1980;

575   Duval et al., 1983; Weertman, 1983,1985; Azuma and Higashi, 1984; Pimienta and Duval, 1987;

576   Budd and Jacka, 1989; Jacka and Li, 1994; Goldsby and Kohlstedt, 2001; Bindschadler et al.,

577   2003; Cuffey, 2006; Chandler et al. 2008; Cuffey and Kavanaugh, 2011; McCarthy et al., 2017;

578   Millstein et al., 2022; Colgan et al., 2023; Li, 2025). The wide range of reported n-values is

579   governed by a complex interplay of deformation mechanisms—including grain boundary sliding,

580   diffusion (lattice and grain boundary), and dislocation processes, e.g. hard-slip-dominated,

581   dislocation-accommodated grain boundary sliding, and grain boundary sliding-limited basal

582   dislocation—across varying stresses, temperatures, crystalographic fabrics, impurity contents, and

583   grain-size-to-sample-size ratios. We attribute the significant discrepancy in these findings to the

584   experimental conditions. The lower temperatures used (down to –30°C) induce slower strain rates,

585 which prevented the tests from reaching a critical strain rate minimum (SRMin). Therefore, to

586 accurately estimate the activation energy for deformation, it is necessary first to calibrate the

587 SRMin value for all noised samples. A constant stress exponent value of $n \approx 4.3$ (Li and Baker,

588 2022a) was used to compute the activation energy. This necessary simplification—an

589 acknowledgement of current methodological limitations rather than a dismissal of the underlying

590 physics—introduces a key uncertainty that highlights the need for future advancements in

591 observational methodology within firn research. To proceed, the post-calibration SRmins for the –

592 5°C and –18°C samples are highlighted in **Table 2** (see **Appendix B** in detail). It is important to

593 note that the stress exponent does not depend on the density of the tested samples, thereby

594 negating any basis for discussing a relationship between the stress exponent and sample density.

595 Instead, variations in stress corresponding to density variations are manifested in the strain rate,

596 ensuring that the derivation of the stress exponent and activation energy remains consistent. From

597 here on we only discuss the applied stress since there is little difference between the effective

598 stress and applied stress for calculating the stress exponent (Li and Baker, 2022a). Based on both

599 the reported range of Q_c and the two observed SRmins at −5°C and −18°C, the SRmins for the

600 −30°C samples are inferred (**Table 2**), using the Arrhenius relation. Also, based on both the

601 observed and inferred SRmins with the upper and lower bounds (**Table 2**), a series of fitted

602 functions are then found between the SRmin and the reciprocal of the temperature (°C), $1/T_c$:

603

604   20-m samples:

$$\begin{cases} \text{SRMin} = -3 \times 10^{-5}/T_c - 7 \times 10^{-7}[R^2 = 0.988; PC1(L\,20)] \\ \text{SRMin} = -3 \times 10^{-5}/T_c - 2 \times 10^{-7}[R^2 = 1; PC1(U\,20)] \\ \text{SRMin} = -1 \times 10^{-5}/T_c - 3 \times 10^{-7}[R^2 = 1; PC2(L\,20)] \\ \text{SRMin} = -9 \times 10^{-6}/T_c - 2 \times 10^{-7}[R^2 = 0.987; PC2(U\,20)] \\ \text{SRMin} = -2 \times 10^{-6}/T_c - 6 \times 10^{-8}[R^2 = 0.998; PC3(L\,20)] \\ \text{SRMin} = -1 \times 10^{-6}/T_c - 3 \times 10^{-8}[R^2 = 0.976; PC3(U\,20)] \end{cases},$$

40-m samples:

$$\begin{cases} \text{SRMin} = -2 \times 10^{-4}/T_c - 4 \times 10^{-6}[R^2 = 0.988; PC1(L\,40)] \\ \text{SRMin} = -2 \times 10^{-4}/T_c - 2 \times 10^{-6}[R^2 = 1; PC1(U\,40)] \\ \text{SRMin} = -6 \times 10^{-5}/T_c - 2 \times 10^{-6}[R^2 = 1; PC2(L\,40)] \\ \text{SRMin} = -6 \times 10^{-5}/T_c - 1 \times 10^{-6}[R^2 = 0.987; PC2(U\,40)] \\ \text{SRMin} = -1 \times 10^{-5}/T_c - 3 \times 10^{-7}[R^2 = 0.998; PC3(L\,40)] \\ \text{SRMin} = -9 \times 10^{-6}/T_c - 2 \times 10^{-7}[R^2 = 0.976; PC3(U\,40)] \end{cases},$$

60-m samples:

$$\begin{cases} \text{SRMin} = -7 \times 10^{-4}/T_c - 2 \times 10^{-5}[R^2 = 0.988; PC1(L\,60)] \\ \text{SRMin} = -6 \times 10^{-4}/T_c - 6 \times 10^{-6}[R^2 = 1; PC1(U\,60)] \\ \text{SRMin} = -2 \times 10^{-4}/T_c - 7 \times 10^{-6}[R^2 = 1; PC2(L\,60)] \\ \text{SRMin} = -2 \times 10^{-4}/T_c - 4 \times 10^{-6}[R^2 = 0.987; PC2(U\,60)] \\ \text{SRMin} = -3 \times 10^{-5}/T_c - 1 \times 10^{-6}[R^2 = 0.998; PC3(L\,60)] \\ \text{SRMin} = -3 \times 10^{-5}/T_c - 7 \times 10^{-7}[R^2 = 0.976; PC3(U\,60)] \end{cases},$$

where PC1(L20) and PC1(U20) indicate the lower and upper bound values of the post-calibration SRmins from the 20 m samples (**Table 1**), and other symbols are similarly formatted, e.g. PC1(L40), PC1(U40), PC1(L60), PC1(U60), and so on. These relationships are plotted in **Figure 8**, where the SRmin vs. $1/T_c$ plots from the three depths are almost the same shape, implying that the SRmin is dependent on the temperature at a constant stress. It is important to note that the average (minimum) strain rate for the secondary creep stage for a given temperature increases with increasing depth/density of the samples (**Figure 8**; **Table 2**). This is opposite to a decrease of

618   the SRmin at a fixed stress and temperature in **Figure 8** and **Table 4** in Li and Baker (2022a).

619   These changes in SRmin are irrespective of the stress (**Appendix A**). The temperature plays a

620   predominant role during firn creep for a given density of sample at a constant stress. An

621   interesting question on firn creep at a specific temperature is whether the SRmin slows down or

622   speeds up with decreasing density of firn. Certainly, natural firn samples raise the complexity in

623   interpreting the firn creep due to the influences both from inclusions (Li and Baker, 2022a and

624   references therein; Li, 2024), and from the topology of the microstructures (Liu et al., 2022). In

625   addition, there is a broad spread of the SRmin at each depth, in which the SRmin varies by several

626   times, even one order of magnitude or more between the different possibilities of post-calibration

627   SRmins (**Figure 8**), implying that the microstructure of the sample significantly influences the
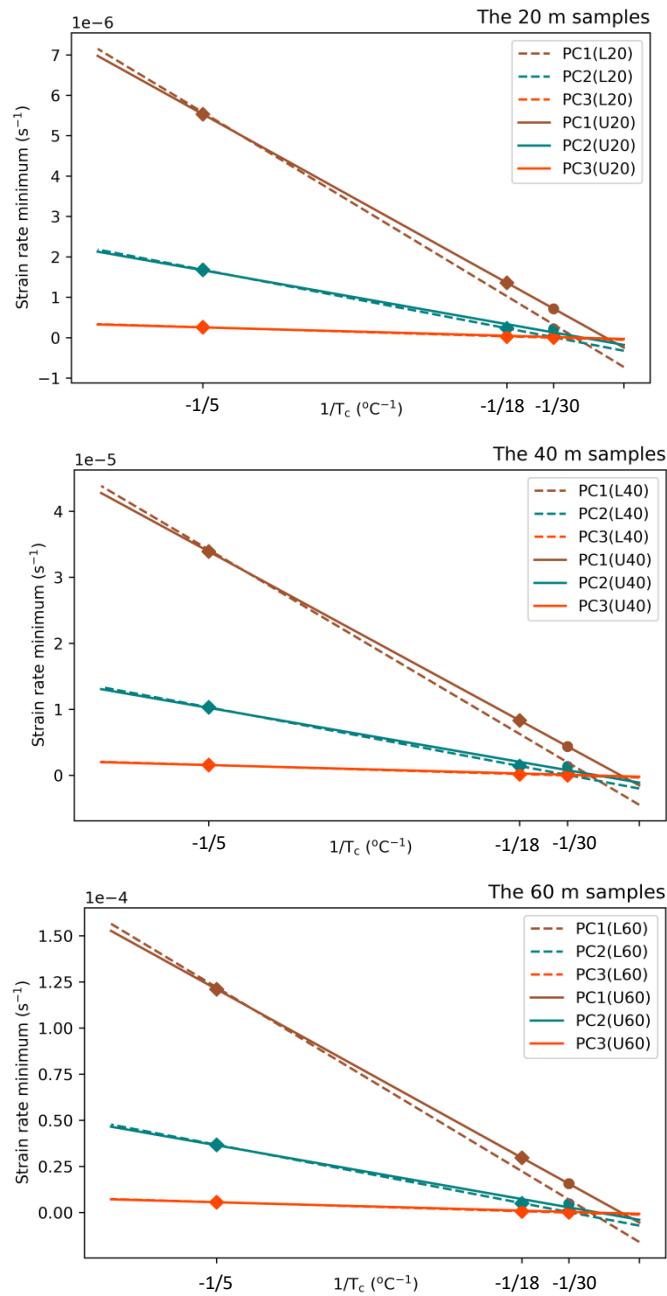
Figure 9: Plots of the strain rate minimum versus the reciprocal of temperature. PC1(L20) and PC1(U20) indicates the lower and upper bound, respectively, from the 20 m samples via PC1 as noted in Table 2, and so on. The circles indicate the upper bound data measured and inferred, while the squares indicate the lower bound data. The dashed line is the fit from the lower bound, while the solid line is the fit from the upper bound.

650

651 process of the creep of firn. Moreover, it is hard to generalize a universal formula for predicting

652 the SRmin at temperatures below −30°C, where the SRmins becomes negative (**Figure 8**). Thus,

653 there is a need for an in-depth understanding of the polar firn creep behavior in secondary creep

654 stage.

655

656 To illustrate the differences between the Q_c values calculated from PC1-SRmin, PC2-SRmin,

657 and PC3-SRmin, we have plotted them in **Figure 7**. Interestingly, the Arrhenius plots of the

658 natural logarithm of strain rate with 1000/T (**Figure 7**) are similar to those observed by Glen

659 (1955) and Homer and Glen (1978), implying that there is no significant difference in the creep

660 mechanism for a temperature range of –30 ºC to –5 ºC (Glen, 1955; Homer and Glen, 1978),

661 where both diffusion via grain-boundary, vacancy or interstitial defects (Barnes et al., 1971;

662 Brown and George, 1996; Nasello et al., 2005; Li and Baker, 2022b), and dislocations contribute

663 to the creep of polar firn.

664

665 **4. Conclusions**

666 Constant-load creep tests were performed on three cylindrical specimens tested from depths of 20

667 m (applied stress 0.21 MPa), 40 m (0.32 MPa) and 60 m (0.43 MPa) at temperatures of –5 ±

668 0.2ºC, –18 ± 0.2ºC, and –30 ± 0.2ºC from a firn core extracted at Summit, Greenland in June

669 2017. The microstructures were characterized before and after creep testing using the micro-CT

670 and thin sections viewed between optical crossed polarizers. It was found that:

671

672 1. Microstructural parameters measured using the micro-CT show that the polar firn densified

673   during the creep compression (e.g. from 685 to 729 kg m^{-3} for the 40 m specimen at -5°C),

674   *viz.*, the TP (from 25.5 to 20.7%), the ECDa (from 0.86 to 0.69 mm), the SSA (from 3.26 to

675   3.02 mm^{-1}), and the SMI (from -1.85 to -2.8) decreased, while the S.Th (from 0.95 to 0.99

676   mm) and the CP (from 0.01 to 0.02%) increased. Anomalies in the microstructures, especially

677   at low temperatures of -18°C and -30°C, are likely due to metamorphism under temperature

678   gradients, the radial dilation effect during firn deformation, the measurement uncertainty of

679   the micro-CT, or the anisotropy and the heterogeneity of natural firn.

680 2. The transient creep behavior of firn at constant stress and different temperatures obeys an

681   Andrade-like law, but, the time exponent *k* of 0.34–0.69 is greater than the 0.33 found for ice.

682   This is due to fewer grain-boundary constraints in porous firn than in ice.

683 3. The secondary creep behavior of firn at constant stress and different temperatures presented

684   here shows that the strain at the SRmin increases with decreasing firn density and increasing

685   creep temperature. In particular, low-density firn during creep at high temperatures shows that

686   the strain at the SRmin, e.g. 11.8% and 7.5% respectively from the 20 m and 40 m specimens

687   at -5°C, is greater than the strain of 3%, which is the maximum found at the SRMin of ice.

688 4. The tertiary creep behavior of firn at constant stress and different temperatures is more easily

689   observed from lower-density specimens at greater effective stresses and higher creep

690   temperatures. The strain softening in tertiary creep is primarily due to recrystallization.

691 5. The apparent activation energy for the firn creep has a wide range of 61.4–102.8 kJ mol^{-1}

692   because the grains in firn slide more easily along more directions in the more porous and

693   heterogeneous structure, the enhanced fluidity from inclusions, and the topological structure

694 of the firn. In addition, the SRmin is a function of the temperature, depending on the

695 microstructure of firn and the inclusion content. The predicted SRmin increases with

696 increasing firn density at a given temperature and is independent of the effective stress. Lastly,

697 there is no significant difference in the creep mechanism at temperatures ranging from -30°C

698 to -5°C.

699

700 The creep of polar firn behaves differently from full-density ice, implying that firn densification is

701 an indispensable process in fully understanding the transformation of snowfall to ice in the polar

702 regions. Observed firn deformation indicates that temperature plays a determined role in firn

703 densification. Thereby, it will be helpful to bridge a gap between the firn temperature and the

704 climate of the past for reconstructing paleoclimate. Also, it will be helpful to apply a confining

705 load to investigate the microstructure of the creep of polar firn with smaller initial particle sizes at

706 low temperatures using the micro-CT. Further studies of interest are to investigate the quantitative

707 relationship between the microstructural parameters and the mechanical behavior of polar firn,

708 and when the onset of recrystallization occurs during creep, as well as verify the SRmin predicted

709 by the relationship of SRmin vs. temperature from the firn specimens at more extensive ranges of

710 stresses and temperatures.

Appendix A: Hydrostatic pressure, the applied stress, and the effective stress

The hydrostatic pressure, p, which varies with temperature, along with the cohesion of the ice and the friction angle between snow particles, plays a significant role in determining the apparent activation energy and, consequently, the strength of the ice (Fish, 1991). It was calculated from the overburden pressure of snow, i.e. $p=\bar{\rho}_f gh$, where $\bar{\rho}_f$ is the average firn density above the depth of interest, *h*, and *g* is the acceleration of gravity. At Summit, p at the depths of 20 m, 40 m, and 60 m was estimated to be ~0.1 MPa, ~0.22 MPa, and ~0.38 MPa, respectively. Note that the slope of the surface of ice sheets and glaciers at Summit is idealized to be zero, i.e., their surfaces are horizontal. The applied stress, σ, is the applied load divided by the cross-sectional area of a sample. The σ at the depths of 20 m, 40 m, and 60 m were 0.21 MPa, 0.32 MPa, and 0.43 MPa, respectively. The effective stress, $\tilde{\sigma}$, is defined as σ divided by the fraction of ice matrix in firn, see in detail from Li and Baker (2022a). Thereby, $\tilde{\sigma}$ is 0.32 MPa (the mean porosity of 34.9%), 0.43 MPa (24.8%), and 0.5 MPa (14.4%) from the 20–60 m samples, respectively. Note that the stresses were vertically loaded on the sample (parallel to the direction of core axis of the sample) in laboratory tests. Ideally, in order to be analogous to the densification of firn in nature, $\tilde{\sigma}$ for laboratory samples from a given depth should be equal to the p of firn *in situ* at an equivalently same depth at Summit, namely $\tilde{\sigma}$/p = 1. However, in consideration of the laboratory timeframe for experiments (Pimienta and Duval, 1987), the stresses applied in laboratory tests are usually higher with a resulting higher rate of deformation than those *in situ*. Thus, to observe the effect of the stress on the creep of firn with different densities at different depths, we designed the following configuration of the $\tilde{\sigma}$/p with depth, *viz.*, 0.32 MPa/~0.1 MPa = ~3.2, 0.43 MPa/~0.22 MPa = ~1.95, and 0.5 MPa/~0.38 MPa = ~1.32 for the samples from the depths of 20 m, 40 m,

733 and 60 m, respectively. In this manner, the decrement of $\tilde{\sigma}/p$ with increasing depth represents

734 the decrease of the effective stress with increasing depth. Also, it's important to note that the

735 strain rates achieved during creep experiments in laboratory settings are 6 to 7 times faster than

736 on ice sheets due to the constraints of conducting experiment in reasonable times, which requires

737 higher loads.

738

739 **Appendix B:** Strain rate minimum inferred via two kinds of constraints

740 To improve the reliability of inferred SRmins, two kinds of constraints were applied. First, the

741 SRmins from the –5°C and –18°C samples are calibrated using Glen's law $\dot{\varepsilon}=A\sigma^n$ with $n = 4.3$

742 (Li and Baker, 2022a). PC1-SRmin, PC2-SRmin, and PC3-SRmin indicate three possibilities of

743 the SRmins that are calculated from the 20 m, 40 m, and 60 m samples via the *only* SRmin

744 observed at a given temperature (Table 2). As an example, for the –5°C samples, there exist three

745 possibilities from three depths. 1) The SRmin observed from the 20 m sample in bold italic font is

746 used to calculate two other SRmins for the 40 m and 60 m samples in the italic font in the column

747 of PC1-SRmin. 2) In the same manner as in scenario 1), the SRmin observed from the 40 m

748 sample is calculated in the column of PC2-SRmin in the bold italic font, and the SRmin observed

749 from the 60 m sample is calculated in the column of PC3-SRmin in the bold italic font. 3) In the

750 same manner as in scenarios 1) and 2), the SRmin is calculated for the –18 °C samples in turn

751 from three depths. Second, the SRMin of the –30°C samples is inferred on the basis of the range

752 of Q_c, i.e., from 44.8 kJ mol^{-1} (upper bound)   to 113 kJ mol^{-1} (lower bound), using the Arrhenius

753 relation.

Data availability

The data supporting the conclusions in this study are available at https://arcticdata.io/catalog.

Author contribution

Y.L. and I.B. designed the experiments and Y.L. carried them out. Y.L. analyzed the data and visualized the relevant results. Y.L. prepared the manuscript with contributions from all co-authors (K.K. and I.B.).

Competing interests

At least one of the (co-)authors is a member of the editorial board of The Cryosphere.

Acknowledgements

This work was sponsored by the National Science Foundation under Arctic Natural Science Grant No. 1743106. Y.L. gratefully acknowledges Ciao Fu for her great support and help in during the COVID-19 pandemic. The authors wish to thank Chris Polashenski, Zoe Courville and Lauren B. Farnsworth at USA-CRREL for their assistance with the storage of the firn cores. We also acknowledge the use of facilities of the Ice Research Laboratory (Director-Erland Schulson) at Dartmouth College. Finally, the authors thank Editor Nanna Bjørnholt Karlsson, Louis Védrine and an anonymous reviewer for their constructive comments, which significantly improved the quality of this manuscript.

References:

Adolph, A.C.C., Albert, M.R., 2014. Gas diffusivity and permeability through the firn column at Summit, Greenland: measurements and comparison to microstructural properties. T. Cryosph., 8, 319–328, doi:10.5194/tc-8-319- 2014.

Albert, M.R., Shultz, E.F. and Perron, F.E., 2000. Snow and firn permeability at Siple Dome, Antarctica. Ann. Glaciol. 31, 353-356.

Alley, R.B., Clark, P.U., Huybrechts, P., Joughin, I., 2005. Ice-sheet and sea-level changes. Sci. 310(5747), 456-60. doi: 10.1126/science.1114613. PMID: 16239468.

Ambach, W., Eisner, H., 1985. Rheological properties of temperate firn. Polarforschung, Bremerhaven, Alfred Wegener Institute for Polar and Marine Research & Germany Society of Polar Research 55(2), 71–77. hdl:10013/epic.29564.d001.

Anderson, D.L., Benson, C.S., 1963. The densification and diagenesis of snow. In: Kingery, W.D. (Ed.), Ice and Snow. Press, Cambridge, Massachusetts, M.I.T, pp. 391–411.

Arnaud, L., Gay, M., Barnola, J.M., Duval P., 1998. Imaging of firn and bubbly ice in coaxial reflected light: a new technique for the characterization of these porous media. J. Glaciol., 44(147), 326-332.

Ashby, M.F., Duval, P. 1985. The creep of polycrystalline ice. Cold Reg. Sci. Technol., 11 (3), 285-300. doi:10.1016/0165-232X(85)90052-7.

Azuma, N., Higashi, A., 1984. Mechanical properties of Dye 3 Greenland deep ice cores. Ann. Glaciol.

Baker, R.W., Gerberich, W.W., 1979. The effect of crystal size and dispersed-solid inclusions on the activation energy for creep of ice. J. Glaciol., 24(90), 179-194.

796 Barnes, P., Tabor, D., Walker, J.C.F., 1971. The friction and creep of polycrystalline ice. Proc. Roy.

797   Soc. Lond. A (324),127-155.

798 Bartelt, P., Von Moos, M., 2000. Triaxial tests to determine a microstructure-based snow viscosity

799   law. Ann. Glaciol., 31, 457-462.

800 Bindschadler, R., King, M., Alley, R., Anandakrishnan, S., Padman, L., 2003. Tidally controlled

801   stick-slip discharge of a West Antarctic ice stream. Ann. Glaciol., 36, 157–162.

802 Brown, D.E., George, S.M., 1996. Surface and bulk diffusion of $H_2^{18}O$ on single-crystal $H_2^{16}O$ ice

803   multilayers. J. Phys. Chem. 100 (38) 15460–15469.

804 Budd, W.F., Jacka, T.H., 1989. A review of ice rheology for ice sheet modelling. Cold Reg. Sci.

805   Technol. 16(2), 107–144. doi: 10.1016/0165-232X(89)90014-1.

806 Burr, A., Ballot, C., Lhuissier, P., Martinerie, P., Martin, C.L., Philip, A., 2018. Pore morphology

807   of polar firn around closure revealed by X-ray tomography, T. Cryosphy., Copernicus, 12(7),

808   2481-2500. 10.5194/tc-12-2481-2018. hal-01864373.

809 Butkovich, T.R., Landauer, J.K., 1960. Creep of ice at low stresses. U.S. Snow, Ice and

810   Permafrost Research Establishment. Research Report 72.

811 Chandler, D., B. Hubbard, A. Hubbard, T. Murray, Rippin, D., 2008. Optimising ice flow law

812   parameters using borehole deformation measurements and numerical modelling. Geophys.

813   Res. Lett., 35, L12502.

814 Chen, M., Chen, Z.D., 1997. Effective stress laws for multi-porosity media. Appl. Math. Mech.,

815   20(11), 1207–1213.

816 Coleou, C., Lesaffre, B., Brzoska, J.B., Ludwig, W., Boller, E., 2001. Three-dimensional snow

817   images by X-ray microtomography, Ann. Glaciol., 32, 75-81.

818 Colgan, W., et al., 2023. Sixty years of ice form and flow at Camp Century, Greenland. J. Glaciol.,
819   69(276), 919–929.

820 Courville, Z., Horhold, M., Hopkins, M. and Albert, M., 2010. Lattice-Boltzmann modeling of the
821   air permeability of polar firn. J. Geophys. Res., Earth Surface, 115(F4).

822 Coussy, O., 2004. Poromechanics. John Wiley & Sons.

823 Cuffey, K.M., 2006. Manifestations of ice microphysical processes at the scale of whole ice sheets.
824   In: Knight, P. (Ed.), Glacier Science and Environmental Change. Blackwell Publishing, 290–
825   300.

826 Cuffey, K.M., Paterson, W.S.B., 2010. The Physics of Glaciers, 4th edited. Elsevier Inc.

827 Cuffey, K.M., Kavanaugh, J.L., 2011. How nonlinear is the creep deformation of polar ice? A new
828   field assessment. Geol., 39(11), 1027–1030.

829 da Silva, M.R., Schroeder, C., Verbrugge, J.C., 2008. Unsaturated rock mechanics applied to a
830   low-porosity shale. Eng. Geol., 97, 42–52.

831 Durham, W.B., Stern, L.A., 2001. Rheological properties of water ice applications to satellites of
832   the outer planets. Annu. Rev. Earth Planet. Sci. 29(1), 295–330.

833 Duval, P., 1981. Creep and fabrics of polycrystalline ice under shear and compression. J. Glaciol.
834   27, 129–140.

835 Duval, P. Ashby, M.F., Anderman, I., 1983. Rate-controlling processes in the creep of
836   polycrystalline ice. The Journal of Physical Chemistry, 87, 4066-4074.

837 Duval, P., Montagnat, M., 2002. Comment on 'Superplastic deformation of ice: experimental
838   observations' by D. L. Goldsby and D. L. Kohlstedt. J. Geophys. Res.: Solid Earth. 107(B4),
839   ECV 4-1–ECV 4-2. doi: 10.1029/2001JB000946.hal-01698732.

840 Ebinuma, T., Maeno, N., 1987. Particle rearrangement and dislocation creep in a snow
841   densification process. J Phys.(Paris), 48,Colloq. C1, 263–269.

842 Ehlers, W., 2002. Foundations of multiphasic and porous materials. In Ehlers Wolfgang and

843   Bluhm J eds. Porous Media– Theory, Experiments and Numerical Applications. Berlin:

844   Springer, pp. 3–86.

845 Eichler, J., 7 others, 2017. Location and distribution of micro-inclusions in the EDML and NEEM

846   ice cores using optical microscopy and in situ Raman spectroscopy. The Cryosphere. 11(3),

847   1075–1090. doi: 10.5194/tc-11-1075-2017.

848 Faria, S.H., Weikusat, I., Azuma, N., 2014. The microstructure of polar ice. Part II: state of the art.

849   J. Struct. Geol. 61, 21–49. doi:10.1016/j.jsg.2013.11.003.

850 Fish, A.M. (1991) Creep and yield model of ice under combined stress. USA Cold Regions

851   Research and Engineering Laboratory, Special Report 91-31.

852 Flin, F., Brzoska, J.B., Lesaffer, B., Coleou, C., Pieritz, R.A., 2004. Three-dimensional geometric

853   measurements of snow microstructural evolution under isothermal conditions. Ann. Glaciol.,

854   38, 39-44.

855 Freitag, J., Dobrindt, U., Kipfstuhl, J., 2002. A new method for predicting transport properties of

856   polar firn with respect to gases on the pore-space scale, Ann. Glaciol., 35, 538-544.

857 Frost, H.J., Ashby, M.F. 1982. Deformation-mechanism maps: the plasticity and creep of metals

858   and ceramics. Oxford: Pergamon Press.

859 Fujita, S., Hirabayashi, M., Goto-Azuma, K., Dallmayr, R., Satow, K., Zheng, J., Dahl-Jensen, D.,

860   2014. Densification of layered firn of the ice sheet at NEEM, J. Glaciol., 60 (223), 905-921,

861   doi:10.3189/2014JoG14J006.

862 Gagliardini, O., Meyssonnier, J., 2000. Simulation of the creep of ice with a self-consistent

863   anisotropic approach. Comput. Mech., 25(5), 479-486.

864 Glen, J.W., 1955. The creep of polycrystalline ice, Proceedings of the Royal Society A, 228(1175),

519-538, doi.10.1098/rspa.1955.0066.

Goldsby, D.L., Kohlstedt, D.L., 1997. Grain boundary sliding in fine-grained ice I. Scr. Mater. 37(9), 1399–1406.

Goldsby, D.L., Kohlstedt, D.L., 2001. Superplastic deformation of ice: experimental observations, J. Geophys. Res., 106(B6), 11017-11030.

Goodman, D.J., Frost, H.J., Ashby, M.F., 1981. The plasticity of polycrystalline ice, Philos. Mag., A43 665–695.

Gow, A.J., 1969. On the rates of growth of grains and crystals in South Polar firn. J. Glaciol., 8(53) 241-252.

Gray, W.G., Schrefler, B.A., 2007. Analysis of the solid stress tensor in multiphase porous media. Int. J. Numer. Anal. Methods Geomech., 31, 541–581.

Goujon, C., J.-M. Barnola, C. Ritz. 2003. Modeling the densification of polar firn including heat diffusion: Application to close-off characteristics and gas isotopic fractionation for Antarctica and Greenland sites, J. Geophys. Res., 108(D24), 4792,doi:10.1029/2002JD003319.

Gubler, H., 1978. Determination of the mean number of bonds per snow grain and of the dependence of the tensile strength of snow on stereological parameters. J. Glaciol., 20(83),329-341.

Hammonds, K., Baker, I., 2016. The effects of Ca++ on the strength of polycrystalline ice. J. Glaciol. 62,1–9. doi: 10.1017/jog.2016.84.

Hammonds, K., Baker, I., 2018. The effects of H_2SO_4 on the mechanical behavior and microstructural evolution of polycrystalline Ice. J. Geophys. Res.: Solid Earth. 123,1–22. doi: 10.1002/2017JF004335.

888 Hansen, B.L., Landauer, J.K., 1958. Some results of ice cap drill hole measurements. IASH Publ.

889 47 (Symposium at Chamonix 1958– Physics of the Movement of the Ice), 313–317.

890 Hansen, A.C., Brown, R.L., 1988. An internal state variable approach to constitutive theories for

891 granular materials with snow as anexample. Mech. Mater., 7(2),109-119.

892 Higashi, A., Konimua, S., Mae, S., 1965. Plastic yielding in ice single crystals. Jpn. J. Appl. Phys.

893 4, 575-82.

894 Hildebrand, T., Ruegsegger, P. 1997. A new method for the model-independent assessment

895 ofthickness in three-dimensional images. J. Microsc., 185, 67-75.

896 Hobbs, P.V., 1974. Ice Physics, 1st edited. Oxford University Press Inc., New York.

897 Homer, D.R., Glen, J.W., 1978. The creep activation energies of ice. J. Glaciol., 21(85), 429-444.

898 Hooke, R.L., Mellor, M., Budd, W.F., Glen, J.W., Higashi, A., Jacka, T.H., Jones, S.J., Lile, R.C.,

899 Martin, R.T., Meier, M.F., Russell-Head, D.S., Weertman, J., 1980. Mechanical properties of

900 polycrystalline ice: an assessment of current knowledge and priorities for research. Cold Reg.

901 Sci. Technol., 3, 263-275.

902 Hooke, R.L., 1981. Flow law for polycrystalline ice in glaciers: comparison of theoretical

903 predictions, laboratory data, and field measurements. Rev. Geophys. Space Phys., 19(4),

904 664–672.

905 Hooke, R.L., 2005. Principles of Glacier Mechanics. Cambridge: Cambridge University Press.

906 Horhold, M.W., 5 others, 2012. On the impact of impurities on the densification of polar firn.

907 Earth Planet. Sci. Lett. 325–326,93–99. doi: 10.1016/j.epsl.2011.12.022

908 Hutter, K., Johnk, K., 2004. Continuum Methods of Physical Modeling: Continuum Mechanics,

909 Dimensional Analysis, Turbulence. Springer Science & Business Media.

910 Jacka, T.H. 1984. The time and strain required for development of minimum strain rates in ice.

911 Cold Reg. Sci. Technol., 8 (3), 261-268. doi: 10.1016/0165-232X(84)90057-0.

Jacka, T.H., Li, J. 1994. The steady state crystal size of deforming ice. *Ann. Glacial.*, 20, 13–18.

Jacka, T.H., Li, J., 2000. Flow rates and crystal orientation fabrics in compression of polycrystalline ice at low temperatures and stresses, Physics of Ice Core Records International Symposium on Physics of Ice Core Records. Shikotsukohan, Hokkaido, Japan, 83-102.

Jonas, J.J., Muller, F., 1969. Deformation of ice under high internal shear stresses. Can. J. Earth Sci. 6(4), 963–968. doi: 10.1139/e69-100.

Jumawan, A.B., 1972. An experimental study of self-diffusion in polycrystalline ice. Diss.Abstr. Int. B 32, 5163–5164 (Abstract).

Kamb, B., 1961. The thermodynamic theory of nonhydrostatically stressed solids. J. Geophys. Res. 66, 259–271.

Khalili, N., Geiser, F. Blight, G.E., 2004. Effective stress in un-saturated soils, a review with new evidence. Int. J. Geomech., 4(2), 115–126.

King, R.F., 1952. Dissertation, Cambridge.

Lade, P.V., Boer, R.V., 1997. The concept of effective stress for soil, concrete and rock. Geotech., 47(1), 61–78.

Landauer, J.K., 1958. The creep of snow under combined stress. Transactions of the society of rheology II. 175-194.

Li, J., Jacka, T.H., Budd, W.F., 1996. Deformation rates in combined compression and shear for ice which is initially isotropic and after the development of strong anisotropy. Ann. Glaciol., 23, 247-252.

Li, Y., Baker, I. 2021. Dynamic observations of the densification of polar firn under compression using a micro-computed tomograph, J. Geophys. Res., Earth Surface,126, e2021JF006290. doi:org/10.1029/2021JF006290.

Li, Y. 2022. Critical values of the microstructural parameters at the first critical density of the densification of polar firn. Cold Reg. Sci. Technol., 198(2022), 10355. doi:org/10.1016/j.coldregions.2022.103553.

Li, Y., Baker, I. 2022a. Observations of the creep of polar firn. J. Glaciol., 68(268), 269–287. doi.org/10.1017/jog.2021.91.

Li, Y., Baker, I. 2022b. Metamorphism observation and model of snow from Summit, Greenland under both positive and negative temperature gradients in a Micro CT, Hydrol. Processes, e14696. doi.10.1002/HYP.14696.

Li, Y. 2023b. Changes in grain size during the relaxation stage of viscoelastic firn, Philos. Mag., 104(4), 239-259. doi.org/10.1080/14786435.2023.2296656.

Li, Y. Fu, C. Keegan, C. et al. 2023. Microstructural characterization of depth hoar and ice-crust layers using a micro-CT, and hypothesis of ice-crust formation under a thunderstorm, Hydrol. Processes, 37(12), e15060. doi.org/10.1002/hyp.15060.

Ligtenberg, S.R.M., Helsen, M.M., van den Broeke, M. R. 2011. An improved semi-empirical model for the densification of Antarctic firn. The Cryosphere, 5, 809–819, doi.org/10.5194/tc-5-809-2011.

Liu, K., Sun, R. & Daraio, C. 2022. Growth rules for irregular architected materials with programmable properties. Sci., 377(6609), 975-981.

Lundin, J.M., Stevens, C.M., Arthern, R., Buizert, C., Orsi, A., Ligtenberg, S.R., et al. 2017. Firn model intercomparison experiment (FirnMICE). J. Glaciol. 63(239), 401–422. https://doi.org/10.1017/jog.2016.114.

Maeno, N., Ebinuma, T., 1983. Pressure sintering of ice and its implication to the densification of snow at polar glaciers and ice sheets. J. Phys. Chem. 87, 4103–4110.

Mahajan, P. and R.L. Brown. 1993. A microstructure-based constitutive law for snow. Ann.

Glaciol.,18, 287-294.

McCarthy, C., Savage, H., Nettles, M., 2017. Temperature dependence of ice-on-rock friction at realistic glacier conditions. J. Glaciol., 63(241), 595–606.

Mellor, M., Smith, J.H., 1966. Creep of snow and ice, CRREL Res. Rep. 220.

Mellor, M., Testa, R., 1969. Effect of temperature on the creep of ice. J. Glaciol., 8(52), 131-145.

Mellor, M., 1975. A review of basic snow mechanics. Int. Assoc. Hydrol. Sci. 114, 251–291.

Meussen, B., Mahrenholtz, O., Oerter, H., 1999. Creep of polar firn. Cold Reg. Sci. Technol. 29, 177–200. doi: 10.1016/S0165-232X(99)00018-X

Millstein, J.D., Minchew, B.M., Pegler, S.S., 2022. Ice viscosity is more sensitive to stress than commonly assumed. Commun. Earth Environ., 3, 57.

Nasello, O.B., Di Prinzio, C.L., Guzman, P.G., 2005. Temperature dependence of "pure" ice grain boundary mobility, Acta Mater., 53(18) 4863-4869, doi: 10.1016/j.actamat.2005.06.022.

Nuth, M., Laloui, L., 2008. Effective stress concept in unsaturated soils: clarification and validation of a unified framework. Int. J. Numer. Anal. Methods Geomech., 32, 771–801.

Ogunmolasuyi, A., Murdza, A., Baker, I. 2023. The onset of recrystallization in polar firn. Geophys. Res. Lett., 50, e2023GL103435. doi.org/10.1029/2023GL103435.

Paterson, W.S.B., Savage, J.C., 1963. Measurements on Athabasca Glacier relating to the flow law of ice. J. Geophys. Res., 68:4537-43.

Paterson, W.S.B., 1977. Secondary and tertiary creep of glacier ice as measured by borehole closure rates, Rev. Geophys. Space Phys., 15, 47–55.

Perutz, M.F., Seligman, G., 1939. A crystallographic investigation of glacier structure and the mechanism of glacier flow. Proc. Roy. Soc. London A 172, 335–360.

Petrenko, V.F., Whitworth, R.W., 1999. Physics of Ice. Oxford: Oxford University Press.

983   Pimienta, P., Duval, P., 1987. Rate controlling processes in the creep of polar glacier ice. Journal

984   de Physique, 48, 243-248.

985   Raymond, C.F., 1973. Inversion of flow measurements for stress and rheological parameters inva

986   valley glacier. J. Glaciol. 12, 19–44.

987   Salamatin, A.N., Lipenkov, V.Y., Barnola, J.M., Hori, A., Duval, P., Hondoh, T. 2009. Snow/firn

988   densification in polar ice sheets. In: Hondoh, T. (Ed.), III. Firn densification, close-off and

989   chronology, 195-222, Hokkaido University Press.

990   Salm, B., 1982. Mechanical properties of snow. Rev. Geophys. Space Phys., 20(N1), 1–19.

991   Scapozza, C., Bartelt, P.A., 2003. The influence of temperature on the small-strain viscous

992   deformation mechanics of snow: a comparison with polycrystalline ice. Ann. Glaciol., 37,

993   90–96.

994   Schleef, S., Lowe, H., Schneebeli, M., 2014. Influence of stress, temperature and crystal

995   morphology on isothermal densification and specific surface area decrease of new snow. T.

996   Cryosphy., 8, 1825-1838.

997   Schwander, J., Sowers, T., Barnola, J.-M., Blunier, T., Fuchs, A., Malaize, B. 1997. Age scale of

998   the air in the summit ice: Implication for glacial-interglacial temperature change, J. Geophys.

999   Res., 102(D16), 19483–19493, doi.org/10.1029/97JD01309.

1000   Simonsen SB, Stenseng L, Adalgeirsdottir G, Fausto RS, Hvidberg CS, Lucas-Picher P. 2013.

1001   Assessing a multilayered dynamic firn-compaction model for Greenland using ASIRAS

1002   radar measurements, J. Glaciol., 59(215), 545–558, doi.org/10.3189/2013JoG12J158.

1003   Sinha, N.K., 1978. Short-term rheology of polycrystalline ice. J. Glaciol., 21(85) 457-472.

1004   Steinemann, S., 1954. Flow and recrystallisation of ice. Proc. Int. Assoc. Hydrol. Sci. 39, 449–

1005   462.

1006   Song, M., Baker, I., Cole, D.M., 2005. The effect of particles on dynamic recrystallization and

fabric development of granular ice during creep. J. Glaciol. 51(173), 377–382. doi: 10.3189/172756505781829287.

Song, M., Cole, D.M., Baker, I., 2006a. Investigation of Newtonian creep in polycrystalline ice. Philos. Mag. Lett. 86(12), 763–771. doi: 10.1080/09500830601023787.

Song, M., Cole, D.M., Baker, I. 2006b. An investigation of the effects of particles on creep of polycrystalline ice. Scr. Mater. 55, 91–94. doi: 10.1016/j.scriptamat.2006.03.029.

Song, M., Baker, I., Cole, D.M., 2008. The effect of particles on creep rate and microstructures of granular ice. J. Glaciol. 54(186), 533–537. doi:10.3189/002214308785836959.

Srivastava, P.K., Mahajan, P., Satyawali, P.K., 2010. A constitutive law for the densification of polar firn. Cold Reg. Sci. Technol., 60(2), 133-138.

Theile, T., Lowe, H., Theile, T.C., Schneebeli, M., 2011. Simulating creep of snow based on microstructure and the anisotropic deformation of ice. Acta Mater. 59, 7104–7113. doi: 10.1016/j.actamat.2011.07.065.

Thomas, R.H., MacAyeal, D.R., Bentley, C.R., Clapp, J.L., 1980. The creep of ice, geothermal heat flow, and Roosevelt Island, Antarctica. J. Glaciol. 25, 47–60.

Treverrow, A., Budd, W.F., Jacka, T.H., Warner, R.C., 2012. The tertiary creep of polycrystalline ice: experimental evidence for stress-dependent levels of strain-rate enhancement. J. Glaciol. 58(208), 301–314. doi: 10.3189/2012JoG11J149.

Vedrine, L., Hagenmuller, P., Gelebart, L., Montagnat, M., Lowe, H. (2025). Sensitivity of the viscoplasticity of polycrystals to porosity and pore-to-crystal size ratio. Acta Materialia, 301, 121507. doi.org/10.1016/j.actamat.2025.121507.

Vickers, W., Greenfield, P., 1968. The high temperature creep properties of compacted magnesium powder. *Journal of Nuclear Materials,* 27(1), 73-79.

1030 Wang, X., Baker, I., 2013. Observation of the Microstructural Evolution of Snow under Uniaxial

1031   Compression using X-ray Computed Micro-tomography, J. Geophys. Res., 118, 1-12,

1032   doi.org/10.1002/2013JD020352.

1033 Weertman, J., 1983. Creep deformation of ice. Annual Review Earth Planet Science, 11, 215–240.

1034 Weertman, J., 1985. Unsolved problems of creep. Nat. 314(6008), 227.

1035 Wiese, M., Schneebeli, M., 2017. Snowbreeder 5: a Micro-CT device for measuring the

1036   snow-microstructure evolution under the simultaneous influence of a temperature gradient

1037   and compaction. J. Glaciol., 63(238), 355–360, doi: 10.1017/jog.2016.143.